The Astrophysical Journal, 575:306–326, 2002 August 10

COLLAPSE OF ROTATING MAGNETIZED MOLECULAR CLOUD CORES AND MASS OUTFLOWS

Kohji Tomisaka
Theoretical Astrophysics, National Astronomical Observatory, Mitaka, Tokyo 181-8588, Japan; tomisaka@th.nao.ac.jp
Received 2001 May 15; accepted 2002 April 10

ABSTRACT

The collapse of rotating magnetized molecular cloud cores is studied with axisymmetric magnetohydrodynamic (MHD) simulations. Because of the change of the equation of state of the interstellar gas, molecular cloud cores experience several phases during the collapse. In the earliest isothermal runaway collapse ($n \lesssim 10^{10}$ H_2 cm^{-3}), a pseudodisk is formed, and it continues to contract until an opaque core is formed at the center. In this disk, a number of MHD fast and slow shock pairs appear whose wave fronts are parallel to the disk. We assume that the interstellar gas obeys a polytropic equation of state with the exponent of $\Gamma > 1$ above the critical density at which the core becomes optically thick against the thermal radiation from dusts $n_{\rm cr} \sim 10^{10}$ cm^{-3}. After the equation of state becomes hard, an adiabatic quasi-static core forms at the center (the first core), which is separated from the isothermal contracting pseudodisk by the accretion shock front facing radially outward. By the effect of the magnetic tension, the angular momentum is transferred from the disk midplane to the surface. The gas with an excess angular momentum near the surface is finally ejected, which explains the molecular bipolar outflow. Two types of outflows are found. When the poloidal magnetic field is strong (its energy is comparable to the thermal one), a U-shaped outflow is formed, in which gas is mainly outflowing through a region whose shape looks like a capital letter U at a finite distance from the rotation axis. The gas is accelerated by the centrifugal force and the magnetic pressure gradient of the toroidal component. The other is a turbulent outflow in which magnetic field lines and velocity fields seem to be randomly oriented. In this case, globally the gas moves out almost perpendicularly from the disk, and the outflow looks like a capital letter I. In this case, although the gas is launched by the centrifugal force, the magnetic force working along the poloidal field lines plays an important role in expanding the outflow. The continuous mass accretion leads to a quasi-static contraction of the first core. A second collapse due to the dissociation of H_2 occurs in it. Finally, another less massive quasi-static core is formed by atomic hydrogen (the second core). At the same time, it is found that another outflow is ejected around the second atomic core, which seems to correspond to the optical jets or the fast neutral winds.

Subject headings: ISM: clouds — ISM: jets and outflows — ISM: magnetic fields — methods: numerical — stars: formation

On-line material: color figures

1. INTRODUCTION

Star formation has been a long-standing target in astrophysics. The infrared protostar distribution revealed that the molecular cloud cores, which coincide with relatively high-density parts ($n \sim 10^4$ cm^{-3}) of the molecular clouds, are the sites of star formation. The observed molecular cloud cores are divided into two categories: those observed associated with and without protostars. The molecular cloud cores without protostars are called starless cores or prestellar cores and are considered younger than those associated with protostars (protostellar cores). From a theoretical point of view, clouds or cloud cores experience the isothermal runaway collapse first, and then accretion onto the stellar core develops (Larson 1969). In the former collapse, the central density increases greatly in a finite timescale (≃free-fall time). A number of prestellar cores show inflow motions (e.g., in L1544, rotation and infall velocities ~0.1 km s^{-1} are observed by Ohashi et al. 1999). This indicates that they are in the dynamically contracting phase, or in other words, in the runaway collapse (Ciolek & Basu 2000). After the epoch when the dust thermal emissions are trapped in the central part of the cloud ($n_c \sim 10^{10}$ cm^{-3}), an adiabatic core is formed at the center, and isothermal gas continues to accrete onto the core. The molecular cloud core in this phase is observed as a protostellar core. It is shown that the dynamical evolution of the cloud core is characterized by the sequence from prestellar cores to protostellar cores.

Dynamical collapse of magnetized clouds has been studied by many authors (Scott & Black 1980; Phillips 1986a, 1986b; Dorfi 1982, 1989; Bentz 1984; Mouschovias & Morton 1991, 1992; Fiedler & Mouschovias 1992, 1993; Basu & Mouschovias 1994; Tomisaka 1995, 1996; Nakamura, Hanawa, & Nakano 1995; Nakamura et al. 1999). Rotating cloud collapse has been attacked seriously with numerical simulations by many authors (Bodenheimer, Tohline, & Black 1980; Norman, Wilson, & Barton 1980; Wood 1982; Narita, Hayashi, & Miyama 1984; Truelove et al. 1997, 1998; Tsuribe & Inutsuka 1999a, 1999b). However, a restricted number of articles have been published regarding the dynamical contraction of the cloud with both rotation and magnetic fields (Dorfi 1982, 1989; Basu & Mouschovias 1994, 1995; Boss 2000, 2001); for quasi-static evolution, see Tomisaka, Ikeuchi, & Nakamura (1990). These researches are confined to the relatively early prestellar stage.

Is it sufficient to consider the effects of the rotational motion and the magnetic fields separately? In the dynamical contraction phase, the molecular outflow is believed to be driven by the cooperative effect of the magnetic fields and rotation motions (Tomisaka 1998). The toroidal magnetic fields are generated from the poloidal ones by the effect of rotation motions (Ampere's law). The torque works only when the poloidal and toroidal magnetic fields coexist, since the Lorentz force in the ϕ-direction works between the poloidal magnetic field and the poloidal current, which makes the toroidal magnetic field. This magnetic torque leads the angular momentum transfer along the magnetic field line, which is important for ejecting the outflow. Since the outflow brings the excess angular momentum, the amount of angular momentum that remains in a protostar and thus in a newborn star is reduced by a factor from 10^{-2} to 10^{-3} from that of the parent molecular cloud core (Tomisaka 2000). Numerical simulations have confirmed that no outflows are observed in the magnetized and nonrotating cloud (Scott & Black 1980; Tomisaka 1996) or the rotating and nonmagnetized cloud (Norman et al. 1980). Therefore, rotation and magnetic fields are both essential to the evolution of molecular cloud cores. In the present paper, we study the dynamical contraction of the magnetized and rotating cloud.

Cooperative effects of magnetic fields and the rotation motions become important after the adiabatic core is formed at the center of the cloud core (Tomisaka 1998). Therefore, the evolution throughout from the prestellar to protostellar core should be studied.

The plan of this paper is as follows: in § 2, the model and numerical method are described. As the initial condition, we choose a slowly rotating cloud threaded by purely poloidal magnetic fields (no toroidal magnetic fields), and we follow the evolution using magnetohydrodynamic (MHD) simulations. Section 3 is devoted to the numerical results. In this section we compare clouds with strong magnetic fields and those with weak magnetic fields. This shows us that two completely different types of outflows are formed in the respective clouds. Another comparison is made between fast and slow rotators. In § 4, we discuss the evolution until the second core, which becomes actually a newborn star, is formed. It is found that another outflow is found around the second core, which seems to correspond to the optical jets or high-speed neutral winds. We also discuss whether the mass inflow/outflow rates and the momentum outflow rates observed in molecular bipolar outflows are explained or not.

2. MODEL AND NUMERICAL METHOD

To study the dynamical contraction, we consider an isothermal cylindrical cloud in hydrostatic balance with infinite length as the initial state. In several star-forming regions, such as the Taurus and Ophiuchus regions, we often find filamentary molecular clouds. However, the relationship is controversial between the direction of the magnetic fields and that of the filament: the ρ Ophiuchi clouds L1709, L1729 (Loren 1989), and L1755 (Goodman et al. 1995) have filamentary shapes, and the directions of the major axes agree with the direction of magnetic field lines, which are measured by the near-IR polarization observations of the background field stars; while in B216–217 clouds in Taurus, the magnetic field lines seem to run perpendicular to the major axes of the dark clouds, even if they seem filamentary (Heyer et al. 1987; Goodman et al. 1992). In this paper, we examine the evolution of these magnetized filamentary clouds. We focus on the model in which magnetic field lines are parallel to the major axis of the filament, and the case with perpendicular magnetic fields will be studied in a separate paper.

In terms of the gravitational potential ψ and the isothermal sound speed c_s, the radial distributions of density ρ, rotation speed v_ϕ, and magnetic field density B_z are calculated using the equation of hydrostatic balance as

$$\frac{v_\phi^2}{r} - \frac{\partial\psi}{\partial r} - \frac{c_s^2}{\rho}\frac{\partial\rho}{\partial r} - \frac{1}{8\pi\rho}\frac{\partial B_z^2}{\partial r} = 0 \tag{1}$$

and the Poisson equation for the self-gravity as

$$\frac{1}{r}\frac{\partial}{\partial r}\left(r\frac{\partial\psi}{\partial r}\right) = 4\pi G\rho \ , \tag{2}$$

where G represents the gravitational constant. This equation has a solution as follows (Stodółkiewicz 1963):

$$\rho_0(r) = \rho_{c0}\left(1+\frac{r^2}{8H_c^2}\right)^{-2} , \tag{3}$$

$$v_{\phi(r)0} \equiv r\Omega_0(r) = r\Omega_{c0}\left(\frac{\rho}{\rho_c}\right)^{1/4} = r\Omega_{c0}\left(1+\frac{r^2}{8H_c^2}\right)^{-1/2} , \tag{4}$$

$$B_{z0}(r) = B_{c0}\left(\frac{\rho}{\rho_c}\right)^{1/2} = B_{c0}\left(1+\frac{r^2}{8H_c^2}\right)^{-1} , \tag{5}$$

with using the scale height at the center,

$$H_c^2 = \frac{c_s^2 + B_{c0}^2/8\pi\rho_{c0}}{4\pi G\rho_{c0} - 2\Omega_{c0}^2} \ , \tag{6}$$

where ρ_{c0}, Ω_{c0}, and B_{c0} represent the density, angular rotation speed, and magnetic flux density, respectively, at the center of the cylindrical cloud ($r = 0$). This is the same hydrostatic configuration studied by Matsumoto, Hanawa, & Nakamura (1997). However, we assume no initial toroidal magnetic field $B_\phi = 0$, in contrast to them. The density distribution is assumed to extend until the radius where the thermal pressure $c_s^2\rho_s$ becomes equal to the external pressure $p_{\rm ext}$, where ρ_s represents the density at the surface of the cylindrical cloud. The solution contains three nondimensional parameters characterizing the distribution after adopting natural normalization such as for distance $r' \equiv r/H \equiv r/[c_s/(4\pi G\rho_s)^{1/2}]$, for time $t' \equiv t/\tau_{\rm ff} \equiv t/[1/(4\pi G\rho_s)^{1/2}]$, and for density $\rho' \equiv \rho/\rho_s \equiv c_s^2\rho(r)/p_{\rm ext}$. We summarize the conversion factors from nondimensional to physical quantities in Table 1. The first parameter characterizing the initial state is related to the magnetic-to-thermal pressure ratio as

$$\alpha \equiv B_z(r)^2/4\pi\rho(r)c_s^2 = B_{c0}^2/4\pi\rho_{c0}c_s^2 \ , \tag{7}$$

where $\alpha = 2/\beta$ if we use the plasma β. The second one is related to the angular rotation speed as

$$\Omega' = \Omega_{c0}/(4\pi G\rho_s)^{1/2} \ . \tag{8}$$

Finally, the third one is the center-to-surface density ratio as

$$F \equiv \rho_{c0}/\rho_s \ . \tag{9}$$

The scale height at the center H_c is rewritten using these

TABLE 1

Conversion from the Nondimensional to the Physical Quantities

Physical Quantities	Conversion Factors	Physical Values ($\mu = 2.33$)
Velocity (m s^{-1})	c_s	190
Density (H$_2$ cm^{-3})	ρ_s	10^2
Length (pc)	$c_s/(4\pi G\rho_s)^{1/2} \equiv H$	$0.341(c_s/190\ \mathrm{m\ s^{-1}})(\rho_s/10^2\ \mathrm{H_2\ cm^{-3}})^{-1/2}$
Time (Myr)	$(4\pi G\rho_s)^{-1/2} \equiv \tau_{\rm ff}$	$1.75(\rho_s/10^2\ \mathrm{H_2\ cm^{-3}})^{-1/2}$
Mass ($M_\odot$)	$c_s^3/(4\pi G)^{3/2}\rho_s^{1/2}$	$0.227(c_s/190\ \mathrm{m\ s^{-1}})^3(\rho_s/10^2\ \mathrm{H_2\ cm^{-3}})^{-1/2}$
Mass accretion rate ($M_\odot$ yr^{-1})	$c_s^3/4\pi G$	$1.29 \times 10^{-7}(c_s/190\ \mathrm{m\ s^{-1}})^3$
	c_s^3/G[a]	$1.62 \times 10^{-6}(c_s/190\ \mathrm{m\ s^{-1}})^3$
Momentum inflow/outflow rate ($M_\odot$ yr^{-1} km^{-1} s^{-1})	$c_s^4/4\pi G$	$2.45 \times 10^{-8}(c_s/190\ \mathrm{m\ s^{-1}})^4$
	c_s^4/G[b]	$3.08 \times 10^{-7}(c_s/190\ \mathrm{m\ s^{-1}})^4$
Magnetic field (μG)	$c_s\rho_s^{1/2}$	$3.75(c_s/190\ \mathrm{m\ s^{-1}})(\rho_s/10^2\ \mathrm{H_2\ cm^{-3}})^{1/2}$

[a] To meet the conventional normalization, we adopt c_s^3/G in § 4.

[b] To meet the conventional normalization, we adopt c_s^4/G in § 4.

nondimensional parameters as

$$H_c'^2 = \frac{H_c^2}{c_s^2/4\pi G\rho_s} = \frac{1+\alpha/2}{F-2\Omega'^2}\ . \tag{10}$$

From this equation, it is shown that a hydrostatic balance is achieved only when $F > 2\Omega'^2$, i.e., $4\pi G\rho_{c0} > 2\Omega_{c0}^2$ in dimensional form. The β-parameter of Matsumoto, Nakamura, & Hanawa (1994), which represents the ratio of the centrifugal force to the thermal pressure force, is expressed using our parameters as

$$\begin{aligned}\beta &= -\frac{\rho(r)v_\phi(r)^2/r}{c_s^2 d\rho(r)/dr}\\ &= \frac{2\Omega_{c0}^2H^2}{c_s^2}\\ &= 2\Omega'^2\frac{1+\alpha/2}{F-2\Omega'^2}\ .\end{aligned} \tag{11}$$

To initiate the cloud collapse, we added density perturbations with a small amplitude. The wavelength of the perturbation is taken equal to that of the most unstable Jeans mode of this isothermal filament. Its linear stability was already studied by Matsumoto et al. (1994). They gave a fitting formula for the most unstable wavelength as follows:

$$\lambda_{\rm max}\left[\frac{c_s}{(4\pi G\rho_s)^{1/2}}\right]^{-1} \simeq \frac{2\pi(1+\alpha/2+\beta)^{1/2}}{0.72\left[(1+\alpha/2+\beta)^{1/3}-0.6\right]F^{1/2}}\ , \tag{12}$$

where we used equations (7), (9), and (11). Therefore, we take this most unstable wavelength, and the initial density is assumed equal to

$$\rho(z,r) = \rho_0(r)\left[1 + A\cos\left(\frac{2\pi z}{\lambda_{\rm max}}\right)\right] \tag{13}$$

for $-\lambda_{\rm max}/2 \le z \le \lambda_{\rm max}/2$. The amplitude of the perturbation A is taken equal to 0.1. Hereafter, we omit the primes which indicate the nondimensional quantities, unless the quantities could be confused with dimensional ones.

From calculations of one-dimensional, nonrotating, nonmagnetized spherical cloud collapse, the effective equation of state of the gas forming a star is summarized as follows (Tohline 1982): the equation of state is determined by the balance between radiative cooling and compressional heating (Masunaga & Inutsuka 1999). Gas in the molecular cloud core with $\rho \sim 10^4$ H$_2$ cm^{-3} obeys the isothermal equation of state with the temperature of $T_0 \sim 10$ K, in which the gas is mainly cooled by the thermal radiation from dust. However, radiative hydrodynamical calculations (e.g., Masunaga & Inutsuka 1999) have shown that the molecular gas becomes optically thick against such emissions, at the density approximately equal to $\rho_c = \rho_{\rm A} \sim 10^{10}$ H$_2$ cm^{-3}. The gas becomes adiabatic beyond the density, and a quasi-hydrostatic H$_2$ core forms that is supported by the thermal pressure (Larson 1969). This is called a first core. In this phase, the polytropic exponent Γ of this molecular hydrogen gas is well approximated equal to 7/5, although Γ is as large as 5/3, while the temperature is quite low, and neither rotational nor vibrational modes of the molecules are excited. The mass of the first core grows by continuous accretion, and the central density and thus temperature increase with time. Finally, hydrogen molecules (H$_2$) dissociate into hydrogen atoms (H) when the core's temperature exceeds $T_{\rm dis} \simeq 10^3$ K. Typical density at which the temperature reaches $T_{\rm dis}$ is equal to $\rho_{\rm B} = \rho_{\rm A}(T_{\rm dis}/T_0)^{1/(\gamma-1)} \simeq 10^{15}\ \mathrm{H_2\ cm^{-3}}(T_{\rm dis}/10^3\ \mathrm{K})^{5/2}(T_0/10\ \mathrm{K})^{-5/2}$. The dissociation ends at the density $\rho_{\rm C} \simeq 10^{19}$ H$_2$ cm^{-3}. Since the hydrogen dissociation reaction absorbs its thermal energy liberated by the compression, the polytropic exponent decreases as $\Gamma \simeq 1.1$. Finally, an atomic hydrogen core is formed, which is called the second core by Larson (1969). Since the constituent of the second core is atomic hydrogen, Γ becomes $\simeq 5/3$. To include these changes, we adopt a multiple polytrope approximation as

$$p = \begin{cases} c_s^2\rho & \rho < \rho_{\rm A}\ ,\\ c_s^2\rho_{\rm A}\left(\dfrac{\rho}{\rho_{\rm A}}\right)^{7/5} & \rho_{\rm A} < \rho < \rho_{\rm B}\ ,\\ c_s^2\rho_{\rm A}\left(\dfrac{\rho_{\rm B}}{\rho_{\rm A}}\right)^{7/5}\left(\dfrac{\rho}{\rho_{\rm B}}\right)^{1.1} & \rho_{\rm B} < \rho < \rho_{\rm C}\ ,\\ c_s^2\rho_{\rm A}\left(\dfrac{\rho_{\rm B}}{\rho_{\rm A}}\right)^{7/5}\left(\dfrac{\rho_{\rm C}}{\rho_{\rm B}}\right)^{1.1}\left(\dfrac{\rho}{\rho_{\rm C}}\right)^{5/3} & \rho > \rho_{\rm C}\ ,\end{cases} \tag{14}$$

with $\rho_A = 10^{10}$ H_2 cm^{-3}, $\rho_B = 10^{15}$ H_2 cm^{-3}, and $\rho_C = 10^{19}$ H_2 cm^{-3}. This is similar to that adopted by Bate (1998). Since the equation of state is achieved by the balance of radiative loss and compressional heating, the result obtained assuming the spherical symmetry might be incorrect if we apply it to the multidimensional simulations. However, as is seen later, the cores (the first and the second cores) are almost spherical, and the approximation of the multiple polytropes is valid.

The basic equations to be solved are the magnetohydrodynamic equations and the Poisson equation for the gravitational potential. In cylindrical coordinates (z, r, ϕ) with $\partial/\partial\phi = 0$, the equations are expressed as follows:

$$\frac{\partial\rho}{\partial t} + \frac{\partial}{\partial z}(\rho v_z) + \frac{1}{r}\frac{\partial}{\partial r}(r\rho v_r) = 0 , \tag{15}$$

$$\begin{aligned}\frac{\partial\rho v_z}{\partial t} &+ \frac{\partial}{\partial z}(\rho v_z v_z) + \frac{1}{r}\frac{\partial}{\partial r}(r\rho v_z v_r)\\ &= -c_s^2\frac{\partial\rho}{\partial z} - \rho\frac{\partial\psi}{\partial z} + \frac{1}{4\pi}\left[-\frac{\partial B_\phi}{\partial z}B_\phi - \left(\frac{\partial B_r}{\partial z} - \frac{\partial B_z}{\partial r}\right)B_r\right] ,\end{aligned} \tag{16}$$

$$\begin{aligned}\frac{\partial\rho v_r}{\partial t} &+ \frac{\partial}{\partial z}(\rho v_r v_z) + \frac{1}{r}\frac{\partial}{\partial r}(r\rho v_r v_r)\\ &= -c_s^2\frac{\partial\rho}{\partial r} - \rho\frac{\partial\psi}{\partial r} + \frac{1}{4\pi}\left[-\frac{1}{r}\frac{\partial}{\partial r}(rB_\phi)B_\phi\right.\\ &\quad\left. + \left(\frac{\partial B_r}{\partial z} - \frac{\partial B_z}{\partial r}\right)B_z\right] ,\end{aligned} \tag{17}$$

$$\begin{aligned}\frac{\partial\rho r v_\phi}{\partial t} &+ \frac{\partial}{\partial z}(\rho r v_\phi v_z) + \frac{1}{r}\frac{\partial}{\partial r}(r\rho r v_\phi v_r)\\ &= \frac{r}{4\pi}\left[\frac{1}{r}\frac{\partial}{\partial r}(rB_\phi)B_r + \frac{\partial B_\phi}{\partial z}B_z\right] ,\end{aligned} \tag{18}$$

$$\frac{\partial B_z}{\partial t} = \frac{1}{r}\frac{\partial}{\partial r}[r(v_z B_r - v_r B_z)] , \tag{19}$$

$$\frac{\partial B_r}{\partial t} = -\frac{\partial}{\partial z}(v_z B_r - v_r B_z) , \tag{20}$$

$$\frac{\partial B_\phi}{\partial t} = \frac{\partial}{\partial z}(v_\phi B_z - v_z B_\phi) - \frac{\partial}{\partial r}(v_r B_\phi - v_\phi B_r) , \tag{21}$$

$$\frac{\partial^2\psi}{\partial z^2} + \frac{1}{r}\frac{\partial}{\partial r}\left(r\frac{\partial\psi}{\partial r}\right) = 4\pi G\rho , \tag{22}$$

where the variables have their ordinary meanings. Equation (15) is the continuity equation; equations (16), (17), and (18) are the equations of motion. The induction equations for the poloidal magnetic fields are equations (19) and (20), and equation (21) is for the toroidal magnetic field. The last equation (22) is the Poisson equation.

The MHD equations are solved using van Leer's (1977) monotonic interpolation and the constrained transport method by Evans & Hawley (1988) with the method of characteristics (MOC) modified by Stone & Norman (1992). This code is based on a hydrocode written from scratch by the author (Tomisaka & Bregman 1993) referring to Norman & Winkler (1986). This is similar to ZEUS2D, which is distributed by NCSA. To ensure that the specific angular momentum $\rho r v_\phi$ and the toroidal magnetic fields B_ϕ are convected similar to the density, advections of such values are calculated using the consistent advection, which was first pointed out by Norman et al. (1980). We rewrite the advection terms of equations (18) and (21) as

$$\frac{\partial B_\phi}{\partial t} = -\frac{\partial}{\partial z}\left[\left(\frac{B_\phi}{\rho}\right)(\rho v_z)\right] - \frac{\partial}{\partial r}\left[\left(\frac{B_\phi}{\rho}\right)(\rho v_r)\right] , \tag{23a}$$

$$\frac{\partial\rho r v_\phi}{\partial t} = -\frac{\partial}{\partial z}\left[(r v_\phi)(\rho v_z)\right] - \frac{1}{r}\frac{\partial}{\partial r}r\left[(r v_\phi)(\rho v_r)\right] . \tag{23b}$$

To evaluate the right-hand side of equations (18) and (21), we choose the same numerical mass flux $\rho\boldsymbol{v}$ as used in equations (15) and (16) and multiply B_ϕ/ρ and $r v_\phi$ by the mass flux to get numerical fluxes for the angular momentum density and the toroidal magnetic fields. To solve the Poisson equation (22), we adopted MILUCGS (modified incomplete LU decomposition preconditioned conjugate gradient squared method; Meijerink & van der Vorst 1977; Gustafsson 1978).

The gravitational contraction proceeds in a significantly nonhomologous way. To see the early-phase evolution, we have to cover a spatially wide region. On the other hand, to see the late-phase evolution, high spatial resolution is needed, especially near the central compact object. These demands conflict with each other. To overcome the difficulty, we adopt the nested grid method (Berger & Oliger 1984; Berger & Colella 1989), similar to our previous series of papers that treated cloud collapse (Tomisaka 1996, 1998, 2000). In this method, a number of levels of grids with different spacings are prepared; finer grids cover the central high-density portion, and coarser ones cover the cloud as a whole. The grids are named as L0 (the coarsest), L1, L2, . . ., and the grid spacing of Ln is chosen equal to half of that of L$n-1$; that is, the grid spacing of Ln is equal to $\Delta z_n = \Delta z_0 2^{-n}$ and $\Delta r_n = \Delta r_0 2^{-n}$. The L0 grid covers the region $-\lambda_{\max}/2 \le z \le \lambda_{\max}/2$ and $0 \le r \le \lambda_{\max}$.

In the nested grid method, a true boundary condition is applied only to the outer boundary of the coarsest grid L0, on which we adopt the fixed boundary condition at $r = \lambda_{\max}$ and the periodic boundary condition at $z = \pm\lambda_{\max}/2$. Adopting the periodic boundary condition means that mass and angular momentum are not removed from the system through the upper and lower boundaries. Even if an outflow is ejected and the Alfvén wave generated by the rotational motions propagates, as long as these do not reach the boundaries the results do not suffer from the boundary condition. This is true for all the models that we calculated. The code has been tested comparing the results obtained with and without the nested grid technique (for details see Tomisaka 1996). The most unstable growth rates of perturbations are slightly different ($\simeq$8%): $\rho_c = 10^4\rho_s$ was attained at $t = 1.25\tau_{\rm ff}$ without the nested grid (but using a relatively large number of grid points, 400 × 400) but at $t = 1.351\tau_{\rm ff}$ in the calculation with the nested grid method. This is mainly due to the fact the eigenfunction of the most unstable mode is as wide as the whole size of the numerical box, and this mode is represented better by a simple calculation with a large number of zones (400 × 400) rather than the L0 grid (64 × 64) of the present scheme. However, after the perturbation has grown to be nonlinear, the growth rate agrees well.

As another test, we calculated the evolution of a model (model A) using a setup in which the number of grid points in one level is increased to 128 × 128, while the number of levels is unchanged. This gives twice higher spatial resolutions than models that will be shown in the next section. Comparing these two, it is found that the time necessary to form the core ($\rho = \rho_A$) is slightly different, as is expected; the calculation with lower resolutions (64×64) gives a longer timescale for core formation ($t_c \simeq 0.7219\tau_{\rm ff}$) than that with higher resolutions (128×128; $t_c \simeq 0.7097\tau_{\rm ff}$), which is consistent with the result of the former test. However, the evolutions after core formation are the same for the two calculations, if we use the time after the core formation epoch, $t - t_c$, instead of t itself. This shows us that the 64×64 grid points in each level are sufficient for discussing the evolution of molecular cloud cores to form stars, if we employ the nested grid technique.

3. RESULTS

3.1. *Dynamical Contraction*

In model A, we calculate the evolution with $\alpha = 1$, $\Omega_0 = 5$, $F = 100$, and $\rho_s = 10^2$ H$_2$ cm^{-3}. We summarize the adopted parameters in Table 2. Similar to the *nonrotational* magnetized cloud (see Figs. 2*b* and 2*c* of Tomisaka 1996), the cylindrical cloud fragments into a prolate spheroidal shape whose wavelength is equal to $\lambda_{\rm max}$. This prolate spheroidal shape coincides with the structure expected from the linear stability analysis by Matsumoto et al. (1994). Next, this density-enhanced region begins to contract along the major axis of the cylindrical cloud, since the magnetic fields are assumed to run parallel to the major axis. Finally, it forms a contracting disk (pseudodisk) perpendicular to the magnetic field lines (Fig. 2*d* of Tomisaka 1996). The snapshot at this stage is shown in Figure 1. Using the conversion factors from nondimensional to dimensional quantities shown in Table 1, the epoch $t = 0.6066\tau_{\rm ff}$ corresponds to 1.06 Myr$(\rho_s/10^2$ H$_2$ cm$^{-3})^{-1/2}$ from the beginning of calculation. The respective panels of Figure 1 have different spatial coverages. Figure 1*a*, which shows L1, represents a global structure of the contracting disk extending horizontally, which is perpendicular to the magnetic field lines. At this epoch, the central density reaches $\rho_c \simeq 10^{8.44}\rho_s$.[1] The figure clearly shows that the cloud continues to collapse. This means that the centrifugal force cannot sustain the cloud collapse. The spatial resolution of L1 is so limited that there seems no internal structures in the contracting disk. However, L5, which has 16 times finer resolution than L1, shows that outward-facing shock fronts extend parallel to the *r*-direction. Fronts near $z \simeq \pm 0.02H$ are the fast-mode MHD shock fronts, because the magnetic fields bend toward the front passing the shock front. We can see another density jump near $z \sim 0.01H$ (hereafter we will omit the sign ± and mention the upper half of each figure since the structure is symmetric).

The shock fronts formed parallel to the disk are known in contracting nonmagnetized rotating isothermal clouds (Norman et al. 1980; Matsumoto et al. 1997). These are not due to the rotation; multiple shock fronts are also found in the contracting magnetized cloud without rotation (Nakamura et al. 1999). However, the situation becomes a bit complicated in this cloud. In the outer region $z \gtrsim 0.02H$, the magnetic field lines run almost vertically ($B_z \gg B_r$ and B_ϕ). Passing the MHD fast shock, in the intermediate region ($0.01H \lesssim z \lesssim 0.02H$), the radial and toroidal components are amplified, and the density increases compared to the outer region. Finally, after passing another front near $z \simeq 0.01H$, the toroidal component B_ϕ decreases. That is, since the magnetic field lines deflect departing from the front at the second front, this is a slow MHD shock. The density range represented in this panel is from $10^{2.3}\rho_s = 10^{4.3}(\rho_s/100$ H$_2$ cm$^{-3})$ H$_2$ cm^{-3} to $10^{7.3}\rho_s = 10^{9.3}(\rho_s/100$ H$_2$ cm$^{-3})$ H$_2$ cm^{-3}. It should be noticed that these shocks occurs in the isothermal gas. This phase is called runaway collapse, in which the central density (ρ_c) increases greatly in a finite timescale.

Figure 1*c* shows the structure represented in L10. Almost all the gas in this figure is isothermal. However, a central small part of the contracting disk ($r \lesssim 6 \times 10^{-4}H$ and $|z| \lesssim 1 \times 10^{-4}H$) enters the polytropic regime with a harder equation of state than the isothermal one. At this stage, we can see that another density jump where many density contour lines are confined locally is forming just outside the polytropic part of the disk. This corresponds to the gas with $\Gamma > 1$, which is seen as a gas $\rho > \rho_A = 10^8$ in nondimensional units. This density jump seems to grow into an accretion shock front, since it is known that an accretion shock forms outside the core when the adiabatic core develops (Larson 1969). This is easily understood as follows: the gas with specific heat ratio $\gamma > 4/3$ has a hydrostatic equilibrium irrespective of its mass. The scale height in the *z*-direction of the core becomes larger than that of the disk. The gas with a harder equation of state forms a spherical static core. Since we assume the multiple polytropic relation for $\rho > \rho_A$ (eq. [14]), the core should be called a polytropic core. However, we will call it an adiabatic core in this paper. This is justified since the core is almost spherical (see § 2) and similar to that obtained by radiative hydrodynamic calculations assuming spherical symmetry (Masunaga & Inutsuka 1999).

Figure 2 shows crosscut views along two axes (along the disk midplane $z = 0$ [panel *a*] and along the *z*-axis $r = 0$ [panel *b*]), which shows how the adiabatic core is formed. The lines with 0.6066 represent the stage shown in Figure 1. At this stage ($t = 0.6066\tau_{\rm ff}$), inflowing gas is almost isothermal ($\rho < \rho_A$). In Figure 2*a*, the radial distributions of the density, the magnetic flux density, and the radial and the toroidal components of velocity are shown. We can see that density and magnetic flux density distributions are approximately expressed by power laws as $\rho \propto r^{-2}$ and $B_z \propto r^{-1}$ except for the central part. At $t = 0.6067\tau_{\rm ff}$, the density in

TABLE 2

Model Parameters

Model	α	Ω_0	ρ_A	ρ_s (H$_2$ cm^{-3})	Polytrope
A.............	1	5	10^8	10^2	Realistic
AH1.........	1	5	10^8	10^2	$\Gamma = 2$
AH2.........	1	5	10^8	10^2	$\Gamma = 5/3$
B..............	1	1	10^8	10^2	Realistic
BH...........	1	1	10^8	10^2	$\Gamma = 2$
CH...........	1	0.2	10^8	10^2	$\Gamma = 2$
DH	0.1	1	10^8	10^2	$\Gamma = 2$
EH...........	0.01	1	10^8	10^2	$\Gamma = 2$
N	0	5	10^8	10^2	Realistic
NH	0	5	10^8	10^2	$\Gamma = 2$
R..............	1	1	10^6	10^4	Realistic

---

[1] The central density obtained by L1 is only $\rho_c \simeq 10^{4.94}\rho_s$. However, this is owing to the restriction of the spatial resolution of L1. Using deep levels of grids, we can obtain the true central density.

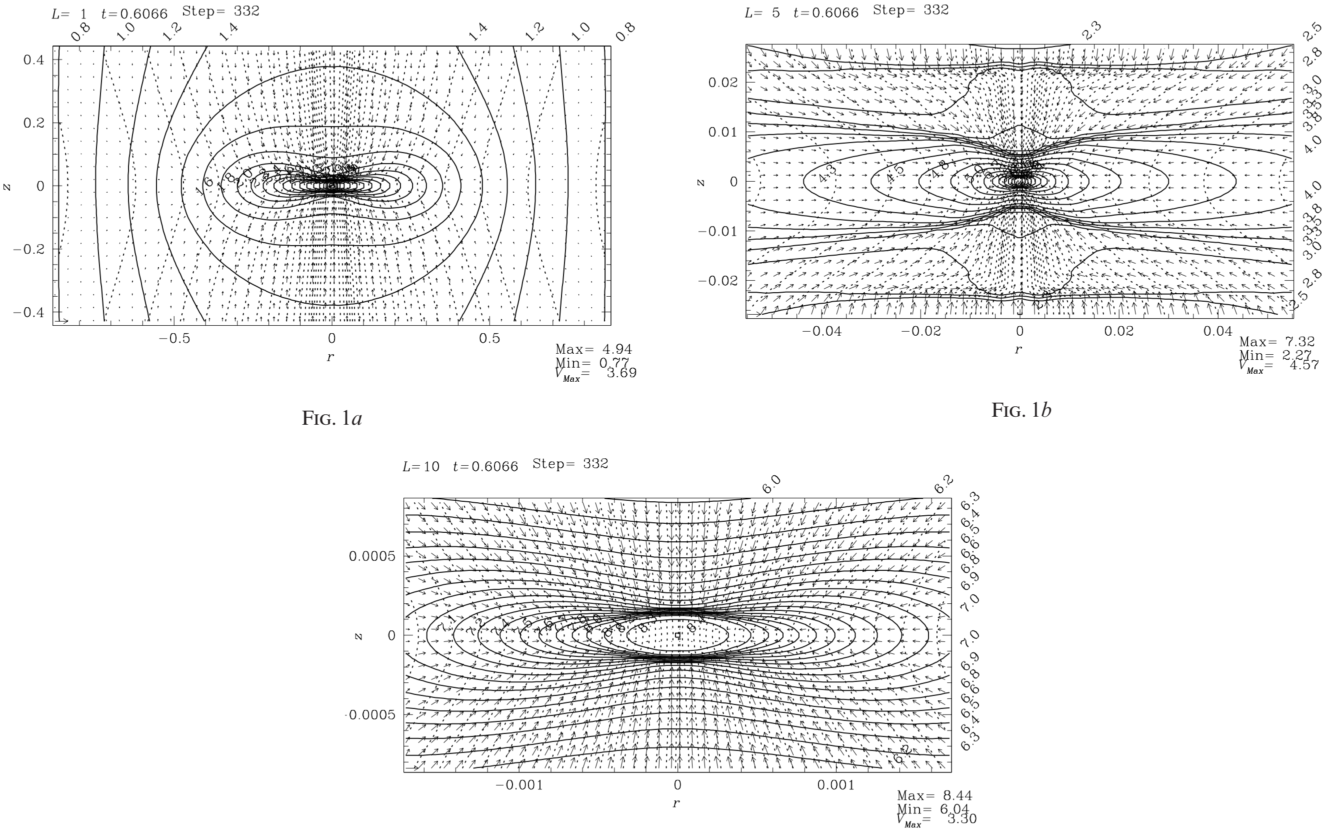

FIG. 1*a*

FIG. 1*b*

FIG. 1*c*

FIG. 1.—Evolution of model A with $\alpha = 1$ and $\Omega_0 = 5$. Snapshots at the time of $t = 0.6066\tau_{\rm ff}$ represented in different levels are shown: L1 (*a*), L5 (*b*), and L10 (*c*). Horizontal and vertical axes represent the *r*- and *z*-axes, of which the units are nondimensional. The actual size of the frames of L5 (*b*) and L10 (*c*) are, respectively, 1/16 and 1/512 smaller than that of L1 (*a*). Magnetic field lines (*dotted lines*) and isodensity contours (*solid lines*) are presented as well as the velocity vectors (*arrows*). Near the bottom right corner, the logarithms of the maximum and the minimum of the densities are numerically shown. Contour levels are chosen for $\log \rho = \log \rho_{\rm min} + n(\log \rho_{\rm max} - \log \rho_{\rm min})/20$ for nondimensional density ρ with $n = 0,\ 1,\ 2,\ \ldots,\ 20$. The maximum speed is also shown, and the velocity vector corresponding to its value is illustrated at the lower left corner by a horizontal arrow. Level, the elapsed time from the beginning, and the number of time steps are shown on the top. The time steps are counted for the coarsest level at that time (L0 for this model). Thus, L1's own time steps are equal to 332×2^1, and L5's are 332×2^5. [*See the electronic edition of the Journal for a color version of this figure. In the electronic version, the magnetic field lines are displayed with red solid lines.*]

the core exceeds $10^9\rho_s = 10^{11}(\rho_s/100\ {\rm H_2\ cm^{-3}})\ {\rm H_2\ cm^{-3}}$, and at $t = 0.6068\tau_{\rm ff}$, it reaches $10^{10}\rho_s = 10^{12}(\rho_s/100\ {\rm H_2\ cm^{-3}})\ {\rm H_2\ cm^{-3}}$. At this stage, a radially outward-facing shock front is seen even inside the disk; infall motion is abruptly decelerated, and the density and magnetic flux density are compressed. This shows that a compact core is formed inside the accretion shock front. The central density increases with time, and inside $r \lesssim 1.8 \times 10^{-4}H$ polytropic gas ($\rho > \rho_{\rm A}$) distributes. The size of the core is equal to $r \sim 1.9 \times 10^{14}(c_s/190\ {\rm m\ s^{-1}})(\rho_s 10^2\ {\rm H_2\ cm^{-3}})^{-1/2}\ {\rm cm} \sim 13 \times (c_s/190\ {\rm m\ s^{-1}})(\rho_s 10^2\ {\rm H_2\ cm^{-3}})^{-1/2}$ AU. This reduces with time since the mass of the core increases by the effect of continuous accretion.

Before the shock front is formed ($t < 0.6067\tau_{\rm ff}$), the radial inflow velocity takes the maximum about $\simeq 2.5c_s$ near $r \simeq 7 \times 10^{-3}H$. For the Larson-Penston self-similar solution for the spherically symmetric dynamical collapse (Larson 1969; Penston 1969), this maximum inflow speed is expected to be equal to $\simeq 3.28c_s$. On the other hand, it equals $\simeq 1.736c_s$ for the nonrotating isothermal *disk* (Saigo & Hanawa 1998). Therefore, it is shown that the actual inflow speed ranges between those expected for the spherically symmetric self-similar solution and for the axially symmetric thin disk solution. After the shock front is formed around the core, the inflow velocity takes the maximum just outside the shock front and the maximum speed increases with time. Inflow motion is accelerated toward the shock front. Similar acceleration is also seen in the toroidal velocity, v_ϕ. Before core formation the toroidal speed v_ϕ takes the maximum $v_\phi \sim 1.7c_s$ near $r \simeq 2.5 \times 10^{-3}H$. However, v_ϕ increases toward the accretion shock after the core formation. At $t = 0.6068\tau_{\rm ff}$ it reaches $v_\phi \simeq 3c_s$ (see also Fig. 1 of Tomisaka 1998).

The structure seen in the crosscut along the *z*-axis is more complicated (Fig. 2*b*). Two shock fronts mentioned earlier (Fig. 1*b*) correspond to the jumps near $|z| \simeq 0.02H$ and $\simeq 0.005H$.[2] At $t = 0.6066\tau_{\rm ff}$, the density and the inflowing velocity distributions have no discontinuities besides these two shock fronts. However, at $t = 0.6067\tau_{\rm ff}$, the inflowing velocity distribution begins to indicate a clear discontinuity near $|z| \simeq 1.5 \times 10^{-4}H$. This shows that a newly formed shock front is propagating spatially. Comparing two curves

---

[2] The shape of the inner slow MHD shock is concave. On the *z*-axis it is found near $z \simeq 0.005H$, while departing from the *z*-axis ($r \gtrsim 0.02H$), it is found near $z \simeq 0.01H$.

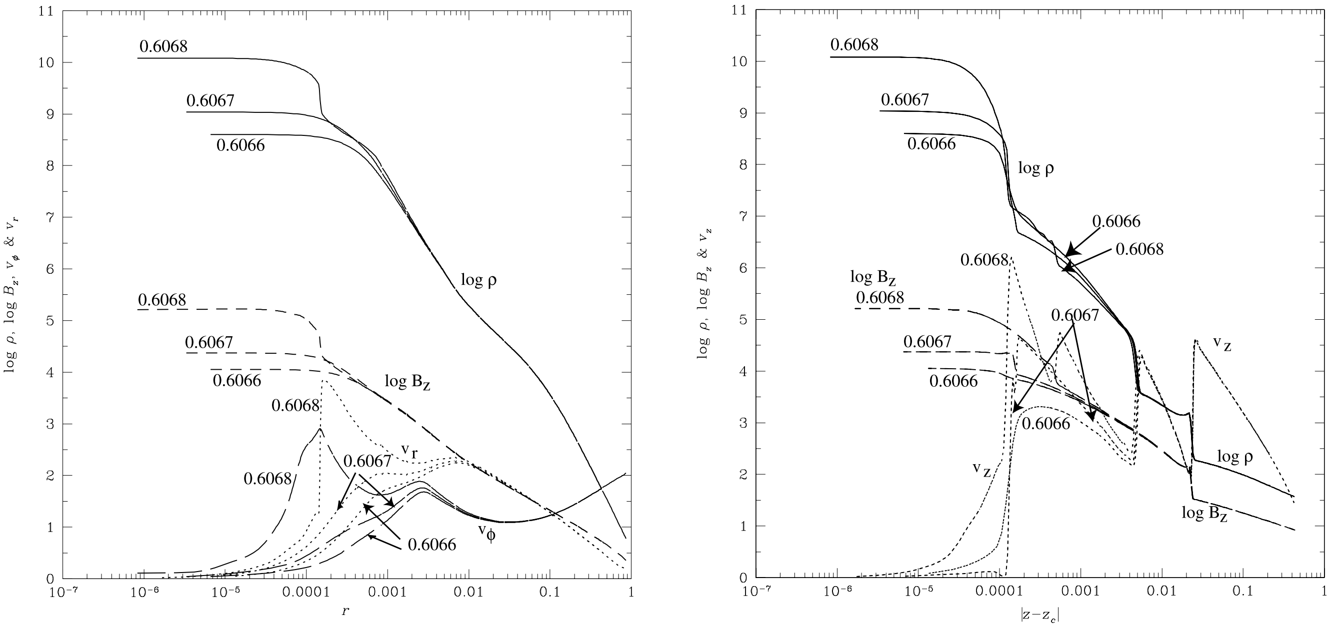

FIG. 2*a*

FIG. 2*b*

FIG. 2.—Crosscut views along the equatorial plane (*a*) and the *z*-axis (*b*). All the dependent and independent variables are those of nondimensional units. The figures show the formation of the first core. In (*a*), $\log \rho(r, z=0)$ (*solid lines*), $\log B_z(r, z=0)$ (*short-dashed lines*), $v_\phi(r, z=0)$ (*long-dashed lines*), and $-v_r(r, z=0)$ (*dotted lines*) are plotted, while in (*b*), $\log \rho(r=0, z)$ (*solid lines*), $\log B_z(r=0, z)$ (*short-dashed lines*), and $-v_z(r=0, z)$ (*dotted lines*) are plotted.

of $t = 0.6067\tau_{\rm ff}$ and $t = 0.6068\tau_{\rm ff}$, it is shown that this shock front breaks into two fronts, and the inner one ($|z| \simeq 1.5 \times 10^{-4}H$) is standing still, while the outer one ($|z| \simeq 5 \times 10^{-4}H$) is propagating outwardly. These two shock fronts are outwardly facing. Thus, the inward propagation of the inner fronts is due to the infalling gas motion.

Figure 2 indicates that the inflow near the *z*-axis is accelerated reaching the central core. Further, comparing v_z for two different epochs, for example, $t = 0.6067\tau_{\rm ff}$ and $t = 0.6068\tau_{\rm ff}$, we can see that the inflow near the *z*-axis is accelerated with time. This is a natural consequence of the fact that the inflow is essentially controlled by the gravity (free fall) in the *z*-direction, which is parallel to the magnetic fields and angular momentum vectors. In this case, accretion speed increases reaching the source of the gravity, and accretion speed also increases with time.

3.2. *Outflow*

Figure 3 illustrates the structure at $t = 0.6069\tau_{\rm ff}$. Although the gas is inflowing both inside and outside of the disk at $t = 0.6067\tau_{\rm ff}$ (Fig. 2), at this stage ($t = 0.6069\tau_{\rm ff}$ [$\tau = 3.2 \times 10^{-4}\tau_{\rm ff}$]),[3] a prominent outflow is formed outside of the disk. This shows that the flow pattern is completely changed in $\Delta t \simeq 2 \times 10^{-4}\tau_{\rm ff} \sim 400$ yr. The outflow sweeps a sphere with a radius of $r \lesssim 1.2 \times 10^{-3}H$ (Fig. 3*a*). Figure 3*b* indicates that the gas near the disk surface flows inwardly for $r \gtrsim 2 \times 10^{-4}H$. However, the direction of the flow is changed upwardly near $r \simeq 2 \times 10^{-4}H$. Finally, this gas is ejected, while the gas flowing near the midplane of the disk ($|z| \lesssim 1 \times 10^{-5}H$) continues to contract. This is reasonable because the total amount of angular momentum in one magnetic flux tube must be conserved in the axisymmetric ideal MHD simulation; for the outflow gas to get angular momentum, a part of the gas in the same magnetic flux tube has to lose its angular momentum and to fall further. In the acceleration process of the gas, the angular momentum is transferred from the gas near the midplane to the gas near the surface of the disk. Considering the angular rotation speed, the angular momentum is transferred from the fast-rotating midplane to the slowly rotating surface gas.

From Figures 1*c* and 3*a* (both show the structure represented in L10), we can see that the magnetic field lines run completely differently comparing before ($\rho_c < \rho_{\rm A}$; Fig. 1*c*) and after ($\rho_c > \rho_{\rm A}$; Fig. 3*a*) the adiabatic core formation. That is, in the isothermal runaway collapse phase (Fig. 1*c*) the magnetic field lines run vertically, in other words, perpendicularly to the pseudodisk. In contrast, after the adiabatic core is formed, the disk continues to contract and drags the magnetic field lines inwardly. Thus, the angle between the magnetic field lines and the disk decreases.

Figure 3*b* is a close-up view whose spatial resolution is 4 times finer than that of Figure 3*a*. This panel shows us that the angle between the flow and the disk is $\simeq 45°$. The reason why the outflow begins only after core formation is related to the angle between the magnetic field lines and the disk, $\theta_{\rm mag}$. Blandford & Peyne (1982) have pointed out that for a cold gas rotating with the Keplerian speed to get angular momentum from the Keplerian disk via infinitely strong magnetic fields, $\theta_{\rm mag}$ must be smaller than a critical value $\theta_{\rm cr} = 60°$. This is understood as follows. Consider the gas in a magnetic flux tube. When the magnetic flux tube is rising steeply from the disk as $\theta_{\rm mag} > \theta_{\rm cr}$, the gas has to climb the effective potential well even if it rotates with the same angular speed as the Keplerian disk. On the other hand, when $\theta_{\rm mag} < \theta_{\rm cr}$, gas can escape from the gravitational well by get-

---

[3] The term t represents the time from the beginning of calculation, but $\tau \equiv t - t_c$ represents the time after core formation. We assume that the core consists of gas with density $\rho > \rho_{\rm A}$.

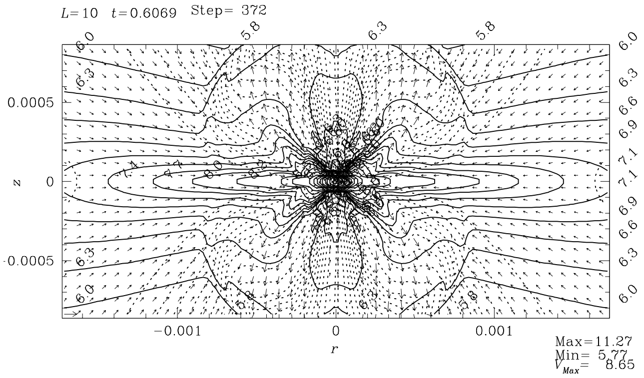

FIG. 3*a*

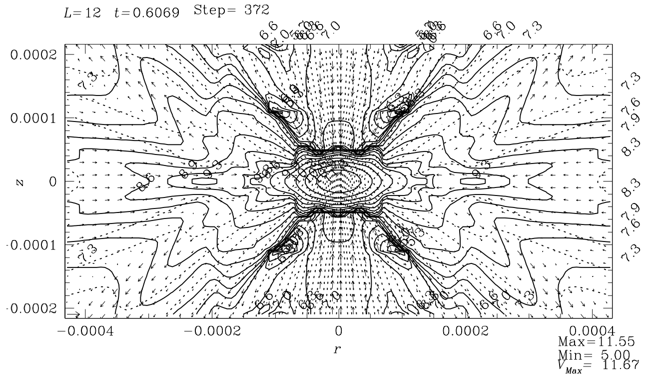

FIG. 3*b*

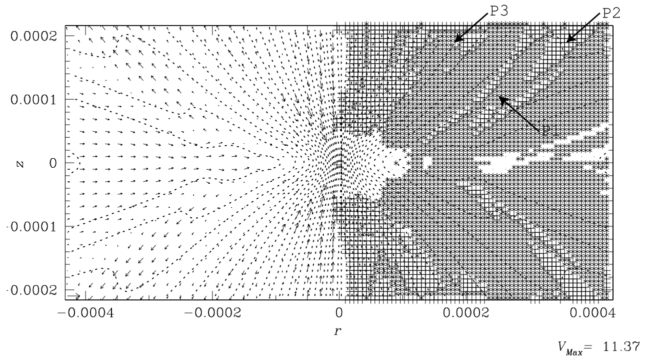

FIG. 3*c*

FIG. 3.—Same as Fig. 1, but for the snapshot at $t = 0.6069\tau_{\rm ff}$. (*a*) Structure represented in L10, which is the same as Fig. 1*c*. At this stage, gas begins to outflow from the disk. Outflow sweeps the sphere $r \lesssim 1.2 \times 10^{-3} H$. (*b*) L12, which has 4 times finer spatial resolution than (*a*). (*c*) Shown is which force is dominant: the thermal pressure gradient, the magnetic force (the toroidal magnetic pressure gradient), or the centrifugal force. The components parallel to the magnetic field are compared for each grid point. The asterisks (*), plus signs (+), and blank spaces indicate the grid points where the centrifugal force is the largest, the magnetic force is the largest, and the thermal pressure gradient is the largest, respectively. On the left, poloidal magnetic field lines and velocity field are shown as in (*b*). [*See the electronic edition of the Journal for a color version of this figure.*]

ting angular momentum from the disk, if the gas has the same angular speed as the Keplerian disk. Although the exact value of $\theta_{\rm cr}$ depends on the disk rotation speed and the disk–to–central star mass ratio, a small angle is preferable for acceleration. This is known as the magnetocentrifugal acceleration mechanism. Kudoh, Matsumoto, & Shibata (1998) have studied a jet ejected from the Keplerian disk with two-dimensional MHD simulations. Using the effective potential defined as

$$\psi_{\rm eff} = \psi - \tfrac{1}{2}\Omega_F^2 r^2 \ , \tag{24}$$

they found that the gas is accelerated after passing the local maximum of this effective potential, when they followed the path of a gas element. (Here Ω_F is the angular velocity of the magnetic field line.) It should be noted that this configuration is achieved only after core formation (Tomisaka 1998).

To explore which force is working to drive the outflow, we calculated the amplitude of respective forces to drive the flow at each grid point: the pressure gradient $-\boldsymbol{\nabla} p$, the magnetic force $(\boldsymbol{\nabla}\times \boldsymbol{B})\times \boldsymbol{B}/4\pi$, and the centrifugal force $\rho v_\phi^2/r\boldsymbol{e}_r$, and we compare their components parallel to the poloidal magnetic field as

$$F_p = -\boldsymbol{\nabla} p \cdot \frac{\boldsymbol{B}_p}{|\boldsymbol{B}_p|} \ , \tag{25}$$

$$F_m = \frac{(\boldsymbol{\nabla}\times \boldsymbol{B})\times \boldsymbol{B}}{4\pi} \cdot \frac{\boldsymbol{B}_p}{|\boldsymbol{B}_p|} \tag{26}$$

$$= -\frac{1}{8\pi r^2}\frac{\boldsymbol{B}_p}{|\boldsymbol{B}_p|} \cdot \boldsymbol{\nabla}(rB_\phi)^2 \tag{27}$$

(Ustyugova et al. 1999), and

$$F_c = \frac{\rho v_\phi^2}{r}\frac{B_r}{|\boldsymbol{B}_p|} \ . \tag{28}$$

Figure 3*c* (*right*) shows the largest force at each grid point. The region filled with asterisks shows the region where the centrifugal force, F_c, dominates over other forces. We will call it region C, which means the centrifugal force–dominated region. An outflow region, which can be seen in the flow vectors displayed in the left half, extending at an angle of $\simeq\pm45°$ to the disk around the point P1 $(z,\ r) \simeq (1 \times 10^{-4} H,\ 2.5 \times 10^{-4} H)$ completely agrees with this region C. Just radially exterior to this region C, there is a region near the point P2 $(z,\ r) \simeq (2 \times 10^{-4} H,\ 3.5 \times 10^{-4} H)$ filled with plus signs where the magnetic force dominates (region M). We can see that the strongest outflow coincides with this region M and the above region C. This means that the outflow is driven by the centrifugal force and the magnetic force (the toroidal magnetic pressure gradient). Another fast outflow found near the point P3 $(z,\ r) \simeq (2 \times 10^{-4}H,\ 1.8 \times 10^{-4}H)$ seems to be driven by the centrifugal force, since this is occupied with another region C. A magnetic force–dominated region (region M) spreads near the z-axis. However, this is an inflow region. At the blank grid points, the thermal pressure gradient is the largest (region T). As a conclusion, it is shown that the gas outflows through the region C and the region M extending from the disk at an angle of $\simeq \pm 45°$.

The toroidal-to-poloidal ratio of the magnetic field strength is as small as $\sim$0.6 in the disk; that is, the disk is poloidal dominated. However, in the region where the gas flows outwardly ($z \gtrsim 5 \times 10^{-4}H$), the toroidal component grows, and the toroidal-to-poloidal ratio reaches $\gtrsim$5–8. In the above regions C and M, which coincide with the strongest outflow, the toroidal magnetic field dominates over the poloidal one. The coincidence of the acceleration region with the toroidal-dominant region seems to indicate that the toroidal fields play an important role in accelerating the gas. This coincidence is understood as follows. The toroidal component of the Lorentz force,

$$F_\phi = \frac{1}{c}(j_z B_r - j_r B_z) = \frac{1}{4\pi}\left(\frac{1}{r}\frac{\partial r B_\phi}{\partial r}B_r + \frac{\partial B_\phi}{\partial z}B_z\right), \quad (29)$$

works mainly below this toroidal-dominant region; that is, $z \lesssim 5 \times 10^{-5}H$. This toroidal component F_ϕ accelerates the toroidal velocity v_ϕ, and the resultant toroidal motion amplifies the toroidal component of the magnetic fields. The rotational motion has the effect of increasing the centrifugal force and forms region C, and the toroidal magnetic field gives a large magnetic pressure gradient. Therefore, it should be concluded that the gas is accelerated by the centrifugal force and the toroidal magnetic pressure gradient, both of which are driven by the rotational motion of the disk. Outflow speed exceeds the sound speed, and the fastest speed reaches $v_{\rm out} \simeq 7.5c_s$ at this time. This increases with time.

3.3. *Effect of the Hardness of the Polytropic Gas*

Although the outflow seems to continue, the further evolution is hard to study, because the timescale (the free-fall timescale at the central core) becomes shorter and shorter. Therefore, we study model AH with a constant polytropic exponent larger than that of model A. In models AH1 (Fig. 4*a*) and AH2 (Fig. 4*b*), the polytropic exponents are chosen as $\Gamma = 2$ and $\Gamma = 5/3$, respectively, for $\rho > \rho_{\rm A}$. (Models whose names have "H" have a simple polytropic relation with $\Gamma = 2$ or $\Gamma = 5/3$ for $\rho > \rho_{\rm A}$.) Because of the hard polytropic exponents, the size of the adiabatic core, whose surface is determined by the jump in v_r, becomes large; for example, at $t = 0.6069\tau_{\rm ff}$ the size is equal to $r_{\rm c} \simeq 4 \times 10^{-4}H$ for model AH1 and $r_{\rm c} \simeq 3 \times 10^{-4}H$ for

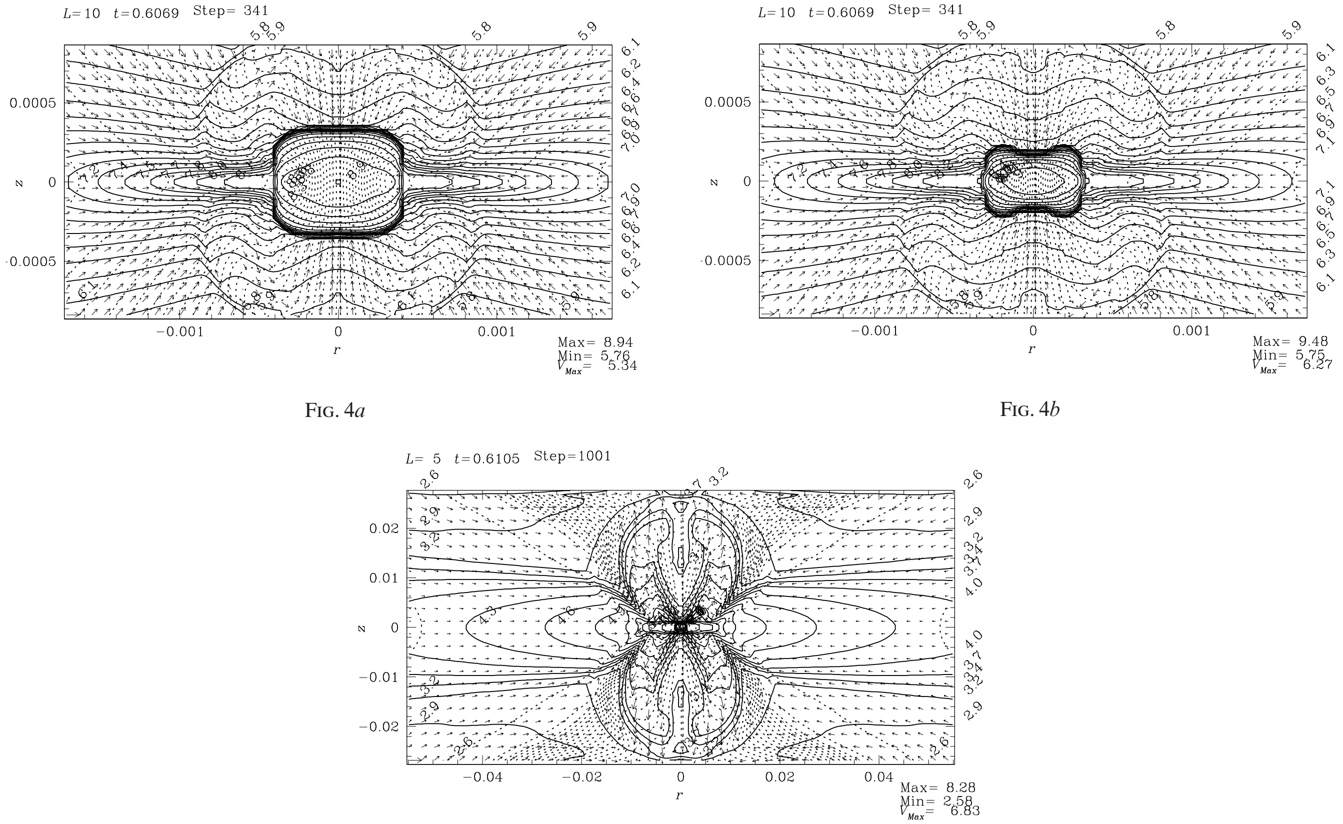

FIG. 4*a*

FIG. 4*b*

FIG. 4*c*

FIG. 4.—Same as Fig. 1, but for models AH1 and AH2. Snapshots at the same epoch as Fig. 3*a*, $t = 0.6069\tau_{\rm ff}$, are shown for models AH1 ($\Gamma = 2$) and AH2 ($\Gamma = 5/3$) in (*a*) and (*b*), respectively. Although the structure of the core is different, the outflow is very similar for each model. In (*c*), the snapshot at $t = 0.6105\tau_{\rm ff}$ ($\tau = 3.94 \times 10^{-3}\tau_{\rm ff}$ from the core formation epoch) is plotted for model AH1. Be careful that the linear size of this panel is 32 times larger than (*a*) and (*b*). Comparing with Fig.1*b* (the same resolution), it is shown that the shock front passed the slow-mode MHD shock and has just reached the outer fast-mode shock front. [*See the electronic edition of the Journal for a color version of this figure.*]

model AH2, while it is equal to $r_c \simeq 1.5 \times 10^{-4}H$ for model A. Similar to model A, just outside the core, outflow begins to be accelerated. The region swept by the outflow expands, and the surface, which separates the inflow and the outflow, forms another MHD shock front. The expansion of the front is very similar to that of model A (the front reaches $z \simeq 1 \times 10^{-4}H$ at this time, which is similar to model A).

To see the similarity in more detail, we calculate the mass of the core,

$$M_{\rm core} \equiv \int_{\rho > \rho_{\rm A}} \rho \, dV \ , \tag{30}$$

for models A, AH1, and AH2. These are equal to $0.1407 c_s^3/(4\pi G)^{3/2}\rho_s^{1/2}$, $0.1504 c_s^3/(4\pi G)^{3/2}\rho_s^{1/2}$, and $0.1450 c_s^3/(4\pi G)^{3/2}\rho_s^{1/2}$ at the time $t = 0.6069\tau_{\rm ff}$ ($\tau = 3.2 \times 10^{-4}\tau_{\rm ff}$) for models A, AH1, and AH2, respectively. At later epoch $t = 0.6085\tau_{\rm ff}$ [$\tau = 2 \times 10^{-3}\tau_{\rm ff} \simeq 3200(\rho_s/10^2 \ {\rm H_2 \ cm^{-3}})^{-1/2}$ yr], $M_{\rm core} \simeq 0.4697 c_s^3/(4\pi G)^{3/2}\rho_s^{1/2} \simeq 0.11(c_s/190 \ {\rm m \ s^{-1}})^3(\rho_s/10^2 \ {\rm H_2 \ cm^{-3}})^{-1/2} \ M_\odot$ (model AH1) and $M_{\rm core} \simeq 0.4104 c_s^3/(4\pi G)^{3/2}\rho_s^{1/2} \simeq 0.09(c_s/190 \ {\rm m \ s^{-1}})^3(\rho_s/10^2 \ {\rm H_2 \ cm^{-3}})^{-1/2} \ M_\odot$ (model AH2). From these results, it is shown that the core mass increases with time because of the continuous accretion and the mass does not depend on the exact equation of state in the core. This is understood as follows: the core mass is determined by the accretion rate of the *isothermal gas*, which is independent from the polytropic exponent Γ in the core.

The gravity by the core has an effect on the outer inflow and outflow. Since the effect depends only on its mass, the difference in the polytropic exponents of the core does not play an important role for the inflow and outflow. Therefore, we will study this model AH to see the long-time evolution of the outflow.

In Figure 4*c*, a snapshot at $t = 0.6105\tau_{\rm ff}$ [$\tau = 4 \times 10^{-3}\tau_{\rm ff} \simeq 7000(\rho_s/10^2 \ {\rm H_2 \ cm^{-3}})^{-1/2}$ yr] is plotted for model AH1. Comparing this with Figure 1*b* for model A (both have the same resolution but for different epochs), it is shown that the shock front that separates the inflow and the outflow passed the slow-mode MHD shock front near $z \simeq 0.01H$ and has just reached the outer fast-mode shock front near $z \simeq 0.02H$. The evolution of model AH2 is essentially the same. The maximum speed of the outflow reaches $\sim 8c_s \sim 2(c_s/0.2 \ {\rm km \ s^{-1}}) \ {\rm km \ s^{-1}}$. This maximum speed seems smaller than that observed in the molecular outflow. Since the mass accumulated in the core is equal to only $\sim 0.1(c_s/190 \ {\rm m \ s^{-1}})^3(\rho_s/100 \ {\rm H_2 \ cm^{-3}})^{-1/2} \ M_\odot$, the outflow speed seems to be much faster than this value, when the mass has grown to that of a typical T Tauri star. Figure 3*b* indicates that the outflow is accelerated near the core and the opening angle of the outflow in this region is wide. However, departing from the acceleration region, the flow changes its direction toward the *z*-axis. Figure 4*c* shows that the opening angle decreases as the outflow proceeds. This indicates that the flow is collimated.

3.4. *Effect of the Initial Rotation Speed*

To see the effect of the initial rotation speed of the cylindrical cloud, we compare models AH1 ($\Omega_0 = 5\tau_{\rm ff}^{-1}$), BH ($\Omega_0 = 1\tau_{\rm ff}^{-1}$), and CH ($\Omega_0 = 0.2\tau_{\rm ff}^{-1}$). These models have the same magnetic field strength, α. In Figures 5*a*–5*c*, the structures at the final epoch of the isothermal runaway collapse phase are plotted for respective models. Models BH and CH indicate no prominent discontinuity in L6 (Figs. 5*b* and 5*c*), while model AH1 has several shock fronts as described in § 3.1. However, in L10 (not shown), there are discontinuities near $z \simeq 6 \times 10^{-4}H$ (model BH) and $z \simeq 5 \times 10^{-4}H$ (model CH) as well as in model AH1 ($z \simeq 1 \times 10^{-4}H$). Comparing panels *b* and *c*, distributions of the density and magnetic field lines are similar. This indicates that the evolution in the isothermal phase is slightly dependent on the initial angular momentum if $\Omega_0 \lesssim 1 \times \tau_{\rm ff}^{-1}$. This seems to correspond to the fact that evolutions of the runaway collapse phase with different initial conditions converge to a self-similar solution (Nakamura et al. 1999).

Figures 5*d*–5*f* show the structure at the age $\tau = 4.5 \times 10^{-3}\tau_{\rm ff}$ after core formation. In all models the outflows are formed. However, the size of the region swept by the outflow is different for each model. With increasing Ω_0, more energetic outflow is driven. From the velocity vectors, it is shown that model AH1 (Fig. 5*d*) forms a bit more collimated outflow than models BH and CH (Figs. 5*e* and 5*f*). This seems to correspond to the differences in density distribution and magnetic field configuration. That is, in model AH1 (also A and AH2), there is a relatively thick disk seen in L6 that is bounded by the shock fronts. This thick disk seems to confine the outflowing gas in model AH1, while in models BH and CH, the disk is relatively thin, which seems to make the flow isotropic. Further, the opening angle of the magnetic field lines in models BH and CH is larger than that of model AH1. This causes the flow also to open.

The difference between models BH and CH comes from the fact that the epochs when outflows begin are different. Since the initial rotation speed in model BH is 5 times larger than that of model CH, in model BH the outflow begins earlier than in model CH. When $\tau \simeq 6 \times 10^{-3}\tau_{\rm ff}$ has passed, however, even in model CH the top of the outflow reaches $z \simeq 0.02H$, and the structure looks very similar to model BH at $\tau \simeq 4.5 \times 10^{-3}\tau_{\rm ff}$ (Fig. 5*e*).

At the epoch when the snapshots of Figures 5*d*–5*f* are taken [$\tau = 4.5 \times 10^{-3}\tau_{\rm ff} \simeq 8 \times 10^3(\rho_s/10^2 \ {\rm H_2 \ cm^{-3}})^{-1/2}$ yr], the mass in the adiabatic core reaches $M_{\rm core} \simeq 0.667 c_s^3/(4\pi G)^{3/2}\rho_s^{1/2}$ (model AH1), $\simeq 1.311 c_s^3/(4\pi G)^{3/2}\rho_s^{1/2}$ (model BH), and $\simeq 1.469 c_s^3/(4\pi G)^{3/2}\rho_s^{1/2}$ (model CH). The instantaneous rate of mass accretion onto the adiabatic core for each model attains $\dot{M}_{\rm acc} \equiv dM_{\rm core}/dt \simeq 110 c_s^3/(4\pi G)$ (model AH1), $\simeq 180 c_s^3/(4\pi G)$ (model BH), and $\simeq 220 c_s^3/(4\pi G)$ (model CH). Therefore, the core mass is approximately proportional to the mass accretion rate, and the mass accretion rate is larger for models with smaller angular rotation speed Ω_0.

The accretion rate expected from the inside-out collapse model (Shu 1977) is equal to $0.975 c_s^3/G = 12.25 c_s^3/(4\pi G)$. Therefore, the accretion rates calculated here are 9–18 times larger than that expected by the inside-out collapse model, while Whitworth & Summers (1985) obtained another self-similar solution, which expresses the evolution after core formation, before which the Larson-Penston self-similar solution is valid for the runaway collapse. Their solution expects an accretion rate of $\simeq 47 c_s^3/G = 590 c_s^3/(4\pi G)$. The observed accretion rates are smaller than that of Whitworth & Summers (1985).

Consider the reason why the mass of the core decreases with increasing Ω_0. Since the gas is supplied to the core mainly through the disk, we consider the mass inflow/outflow transport in the disk. The gas disk can be divided into

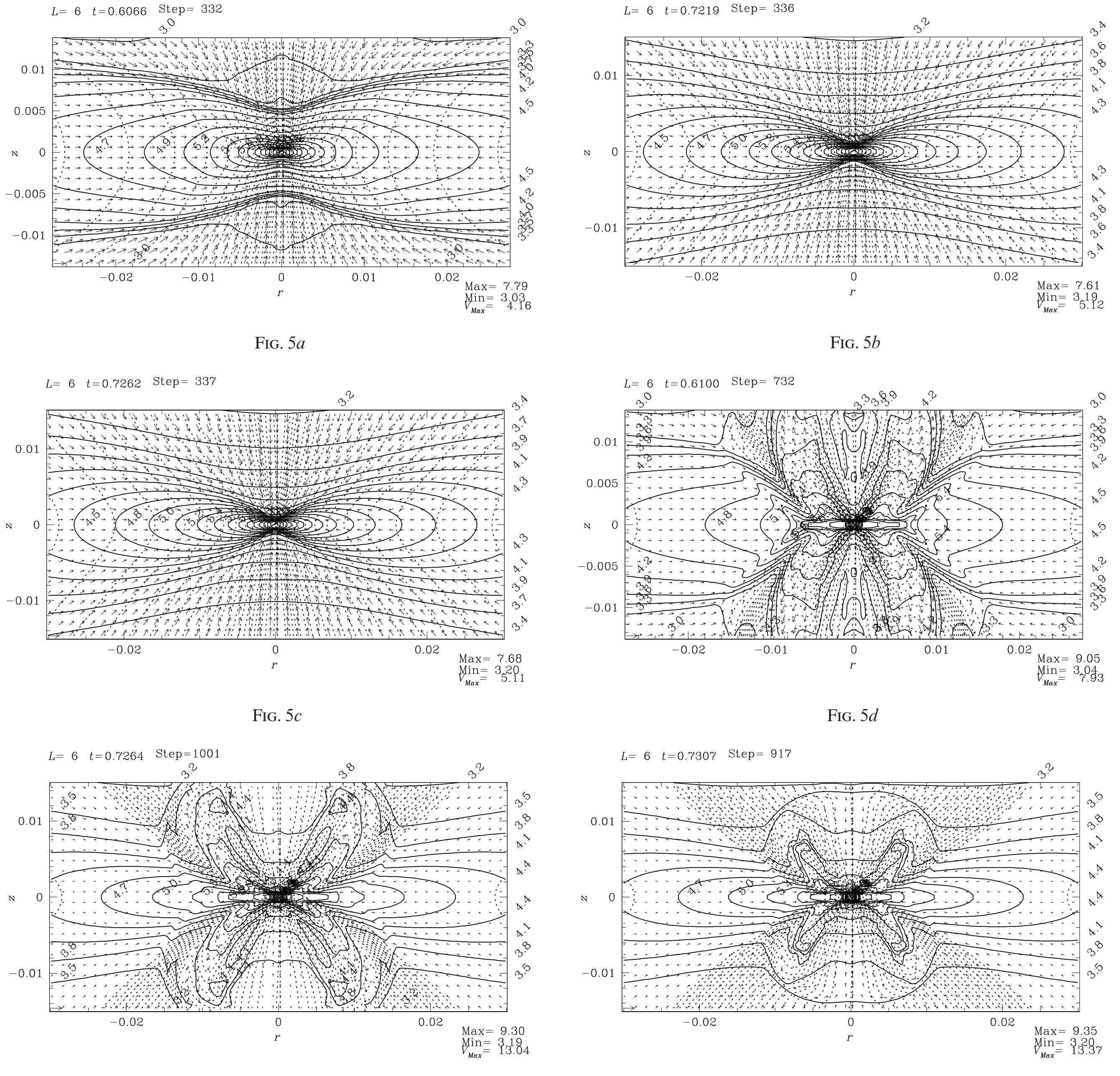

FIG. 5*a*

FIG. 5*b*

FIG. 5*c*

FIG. 5*d*

FIG. 5*e*

FIG. 5*f*

FIG. 5.—Comparison of models with the same magnetic field strength, α, but different rotation speeds, Ω_0. Panels *a* and *d* represent the structure of model AH1 ($\Omega_0 = 5\tau_{\rm ff}^{-1}$) captured by L6. Panels *b* and *e* are for model BH. Model B corresponds to a slower rotator $\Omega_0 = 1\tau_{\rm ff}^{-1}$. Panels *b* and *e* represent the structure captured by L6 at the ages of $t = 0.7219\tau_{\rm ff}$ and $t = 0.7264\tau_{\rm ff}$ ($\tau = 4.5 \times 10^{-3}\tau_{\rm ff}$), respectively. Panels *c* and *f* are for model CH ($\Omega_0 = 0.2\tau_{\rm ff}$) and show the snapshots at $t = 0.7262\tau_{\rm ff}$ and $t = 0.7307\tau_{\rm ff}$ ($\tau = 4.5 \times 10^{-3}\tau_{\rm ff}$), respectively. [*See the electronic edition of the Journal for a color version of this figure.*]

three regions. The outermost region is occupied with isothermal gas, and the gas is contracting or inflowing (pseudodisk). Therefore, the inflow mass rate $(\dot{M}_{\rm in})_{\rm outermost} > 0$, and the outflow mass rate $(\dot{M}_{\rm out})_{\rm outermost} = 0$ in this outermost region. Inside this region, outflow is generated, although a large part of the gas is still inflowing. Therefore, in this middle region, the inflow rate is smaller than that of the outermost region, $(\dot{M}_{\rm in})_{\rm middle} \lesssim (\dot{M}_{\rm in})_{\rm outermost} \simeq (\dot{M}_{\rm in})_{\rm middle} + (\dot{M}_{\rm out})_{\rm middle}$, and the excess mass is transported to the outflow, $(\dot{M}_{\rm out})_{\rm middle} > 0$. Innermost is the adiabatic core. Since the mass accretion rate to the core is equal to the net mass inflow rate from the middle region, $\dot{M}_{\rm acc} \simeq (\dot{M}_{\rm in})_{\rm middle}$.

Mass inflow driven by self-gravity becomes more important in a model with small Ω_0 in which self-gravity is ineffectively counterbalanced with centrifugal force. Therefore, $(\dot{M}_{\rm in})_{\rm outermost}$ becomes larger for a slow rotator. This is the first effect of the rotation.

Furthermore, the outflow brings away an appreciable amount of gas. As mentioned previously, the outflow is strongly generated in the fast rotator. Thus, the mass outflow rate increases with increasing Ω_0 as $(\dot{M}_{\rm out})_{\rm middle} \sim 80c_s^3/(4\pi G)$ (model AH1), $\sim 20c_s^3/(4\pi G)$ (model BH), and $\sim 10c_s^3/(4\pi G)$ (model CH). As a result, increasing Ω_0, the proportion of outflow gas to inflow gas $(\dot{M}_{\rm out})_{\rm middle}/(\dot{M}_{\rm in})_{\rm middle}$ becomes as large as $\sim$40% for model AH1, compared with $\sim 10\%$ for model BH and $\lesssim 5\%$ for model CH. These two effects work cooperatively to reduce the mass accretion rate $\dot{M}_{\rm acc} \simeq (\dot{M}_{\rm in})_{\rm middle}$ to the core for the cloud with large Ω_0.

The maximum outflow speeds realized in the respective figures are equal to $V_{\rm max} \simeq 9.3 c_s$ (model AH1), $6.4 c_s$ (model BH), and $3.2 c_s$ (model CH). Since the outflow is accelerated by the effect of the toroidal magnetic fields that are generated by the rotation motion, this $V_{\rm max}$ increases with increasing Ω_0.

As shown in Tomisaka (2000), since the excess angular momentum of the inflowing gas is effectively removed by the outflow, the total angular momentum of the first core, which is defined as a gas with $\rho > \rho_{\rm A}$, is equal to $j_{\rm core} \simeq 9.2 \times 10^{-5} c_s H$ contained in a mass of $M_{\rm core} = 0.67 c_s^3/(4\pi G)^{3/2} \rho_s^{1/2}$ (model AH1), $\simeq 2.5 \times 10^{-6} c_s H$ in $M_{\rm core} = 1.31 c_s^3/(4\pi G)^{3/2} \rho_s^{1/2}$ (model BH), and $\simeq 7.4 \times 10^{-6} c_s H$ in $M_{\rm core} = 1.47 c_s^3/(4\pi G)^{3/2} \rho_s^{1/2}$ (model CH). The total angular momenta contained in the first cores with $M_{\rm core}$ are only 1.1%, 0.07%, and 0.9% of the initial ones for the respective models.

3.5. *Effect of the Magnetic Field Strength*

To see the effect of the magnetic field strength, we compare models NH, BH, DH, and EH, in which we take $\alpha = 0$, 1, 0.1, and 0.01, respectively.

3.5.1. *Model without Magnetic Fields*

Model NH has no magnetic fields. In Figure 6*a*, a snapshot at $t = 0.6977 \tau_{\rm ff}$ captured by L8 is shown for this model. At this stage, the whole cloud is in the isothermal regime, and the disk experiences runaway collapse even if the centrifugal force works to support the cloud. This confirms the earlier results obtained in 1980s by Norman et al. (1980) and Narita et al. (1984). The physical reason why the centrifugal force does not stop the contraction in the isothermal runaway collapse phase is explained in Hayashi (1987) as follows: because of the centrifugal force, the mass contained in the Jeans scale $[\sim c_s/(G\rho_c)^{1/2}]$ from the center is *decreasing* throughout the collapse. In this sense the centrifugal force does work! Only a small part of the cloud that resides near the center becomes high density. But, the contraction itself continues, and the central density rises greatly in a finite timescale, as long as the isothermal equation of state is valid.

Similar to the previous magnetized models, after the polytrope becomes hard ($\Gamma > 1$), a small adiabatic core is formed first. Since there is no magnetic field, magnetic braking does not work, however, in this model. Therefore, gas accreting onto the core must have a relatively large angular momentum in contrast to the magnetized model. As a result, a centrifugally balanced ring forms by the gas that accreted onto the adiabatic core. The specific angular momentum of the gas increases with the distance from the center. Since the specific angular momentum ($j \equiv r v_\phi$) of newly accreted matter increases further with time, the radius of the centrifugal ring grows radially. Another snapshot in Figure 6*b* at $t = 0.7011 \tau_{\rm ff}$ ($\tau \simeq 3.4 \times 10^{-3} \tau_{\rm ff}$) shows the ring clearly. The ring seems unstable for nonaxisymmetric perturbations. This may form a spiral structure similar to that found by Klein et al. (1999). However, this is beyond the scope of this paper. Therefore, it is concluded that a rotating but nonmagnetic cloud leads to a rotating ring after core formation.

3.5.2. *Models with Magnetic Fields*

To see the effect of the magnetic field strength, in Figure 7 we compare models BH ($\alpha = 1$), DH ($\alpha = 0.1$), and EH ($\alpha = 0.01$). All models have the same initial rotation speed $\Omega_0 = 1$ and the polytropic exponent $\Gamma = 2$. In panels *a*–*c*, the structures at the core formation epoch are plotted. Comparing these with each other, it is shown that in model BH ($\alpha = 1$) a flare-up disk is formed whose isodensity lines are departing from the disk midplane as they leave the center. Decreasing the initial magnetic field strength from model BH to model EH, the shape of dense part of the disk becomes rounder. A similar effect is already reported for nonrotating magnetized cloud collapse (Tomisaka 1996); that is, deceasing α, the shape of the isothermal contracting disk becomes rounder and finally forms a sphere for $\alpha = 0$.

In Figure 7*d* we plot a snapshot for model BH at $t = 0.7264 \tau_{\rm ff}$ ($\tau = 4.46 \times 10^{-3} \tau_{\rm ff}$) represented in L7. This is the same as illustrated in Figure 5*e* but for L7, which has twice as fine spatial resolution as Figure 5*e*. Figure 7*d*, which shows the structure near the root of the outflow, indicates that this is very similar to that of model AH1. For example, the outflow leaves from the disk in the direction almost

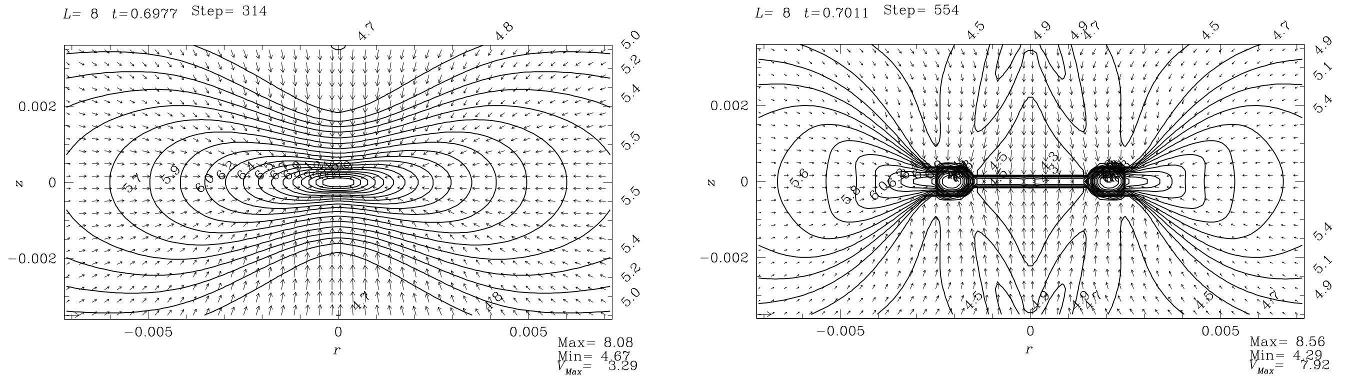

FIG. 6*a* FIG. 6*b*

FIG. 6.—Same as Fig. 1, but for model NH. This model is for a nonmagnetized cloud. In (*a*), a snapshot at $t = 0.6977 \tau_{\rm ff}$ represented in L8 is shown. At this stage, the whole cloud is in the isothermal regime. Another snapshot at $t = 0.7011 \tau_{\rm ff}$ is shown in (*b*). Accreted gas forms a ring that is supported essentially by the centrifugal force.

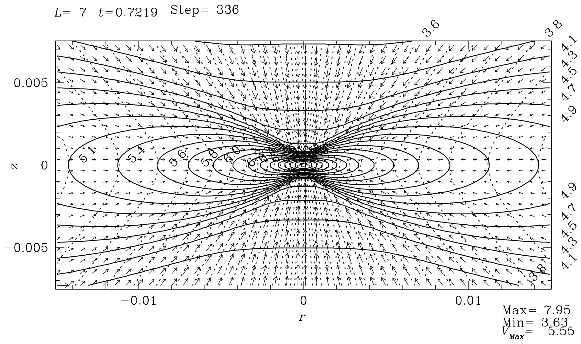

FIG. 7*a*

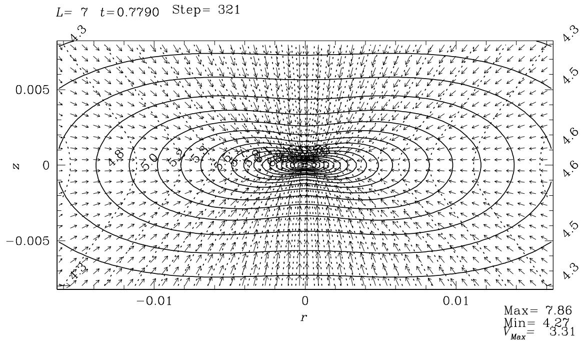

FIG. 7*b*

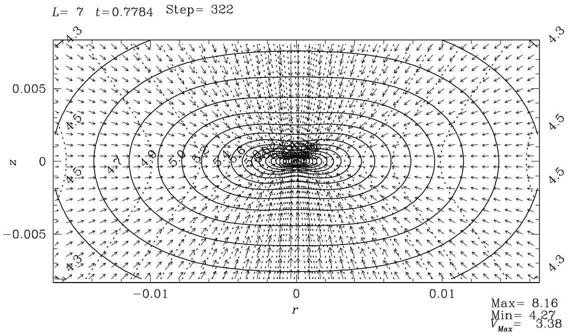

FIG. 7*c*

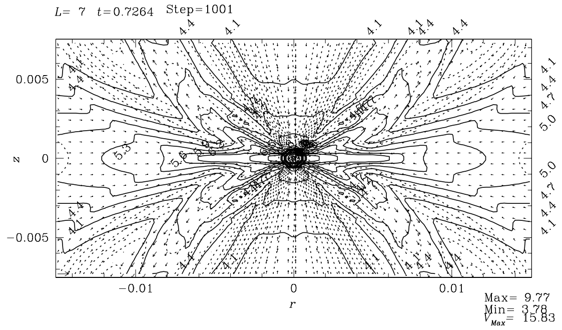

FIG. 7*d*

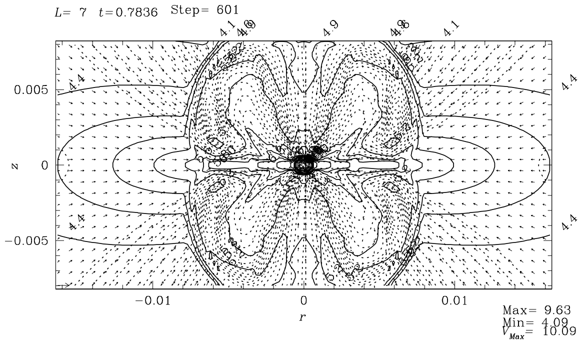

FIG. 7*e*

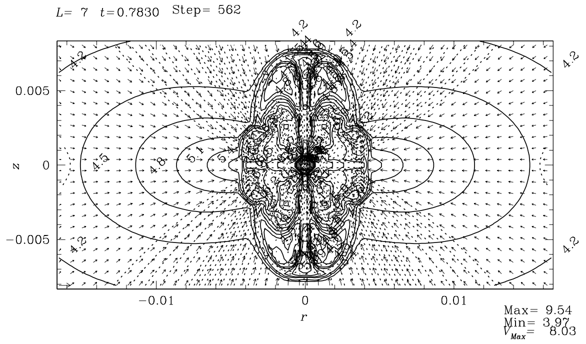

FIG. 7*f*

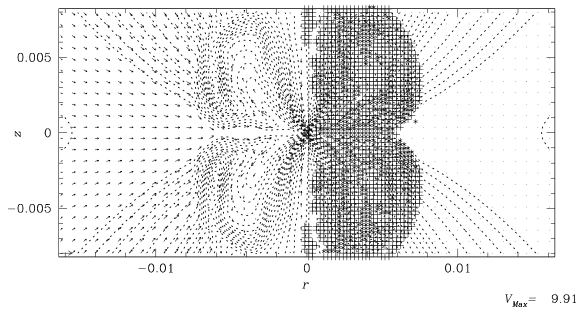

FIG. 7*g*

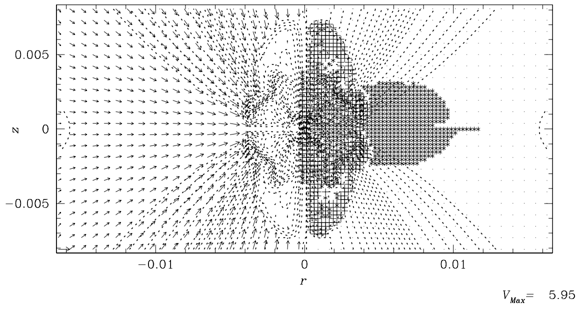

FIG. 7*h*

FIG. 7.—Comparison of models with the same rotation speed, $\Omega_0 = 1$, but different magnetic field strengths, α. Panels *a*, *b*, and *c* represent the structure when the adiabatic core begins to form, while panels *d*, *e*, and *f* represent the structure after a protostar is formed. In panel *a*, we plot a snapshot for model BH captured by L7 at $t = 0.7219\tau_{\rm ff}$, which is the same snapshot shown in Fig. 5*b* but for different level. Panel *d* represents the structure of the same model but for the protostellar phase, that is, $t = 0.7264\tau_{\rm ff}$ ($\tau = 4.46 \times 10^{-3}\tau_{\rm ff}$). This corresponds to Fig. 5*e*. Panels *b* and *e* illustrate snapshots at $t = 0.7790\tau_{\rm ff}$ and at $t = 0.7836\tau_{\rm ff}$ ($\tau = 4.59 \times 10^{-3}\tau_{\rm ff}$), respectively, for model DH ($\alpha = 0.1$). Panels *c* and *f* are for a model with extremely weak magnetic fields (model EH; $\alpha = 0.01$). The snapshots at the epoch $t = 0.7784\tau_{\rm ff}$ and $t = 0.7830\tau_{\rm ff}$ ($\tau = 4.53 \times 10^{-3}\tau_{\rm ff}$) are illustrated in panels *c* and *f*, respectively. Panels *g* and *h* are the same figure as Fig. 3*c* but for models DH and EH. Panel *g* shows the distribution at the same epoch as panel *e*. This indicates that near the disk the centrifugal force dominates (region C) $|z| \lesssim 5 \times 10^{-3}H$. Above $|z| \gtrsim 5 \times 10^{-3}H$, region M is mainly distributed. Compared with Fig. 3*c* of model A, the magnetic force plays a more important role for models with low α. Panel *h*, which shows the force distributions at the same epoch as panel *f*, indicates that the magnetic force–dominated region is predominantly distributed in the magnetic bubble for $|z| \gtrsim 3 \times 10^{-3}H$. This means that the magnetic force plays a major role in the magnetic bubble for model EH. [*See the electronic edition of the Journal for a color version of this figure.*]

parallel to the disk, but it changes its direction to the z-direction. This figure shows that in a timescale of $\tau \simeq 4.5 \times 10^{-3}\tau_{\rm ff}$, the flow pattern is completely changed from the runaway collapse to the outflow plus continuous inflow in the disk. The outflow gas flows through a region whose shape resembles a capital letter U. The outflow departs from the disk with a wide opening angle, but it changes its direction parallel to the z-axis.

In Figure 7*e*, we plot the structure expected for a model with weaker magnetic fields (model DH; $\alpha = 0.1$ and $\Omega_0 = 1$). The snapshot corresponds to the epoch of $t = 0.7836\tau_{\rm ff}$. This corresponds to $\tau = 4.59 \times 10^{-3}\tau_{\rm ff}$, which is similar to the timescale between panels *a* and *d*. In contrast to the previous model BH, the outflow gas is observed to form a sphere, and the magnetic field lines are folded inside this sphere. The magnetic field lines are folded by the pinch or the hoop stress by the toroidal magnetic field. The toroidal magnetic field component is the strongest in the regions where the adjacent poloidal magnetic field lines are running in the opposite directions, for example, the regions around $(z, r) \sim (0.003H, 0.004H)$ and $(z, r) \sim (0.003H, 0.006H)$ in Figure 7*e*.

In this model, the initial poloidal magnetic fields are weak compared to the previous model, BH. Therefore, rotation motion amplifies the toroidal fields, and their strength surpasses easily that of the poloidal ones. Thus, the hoop stress by the toroidal field pinches efficiently the poloidal magnetic field lines. In the outflow acceleration region, the toroidal component is predominant over the poloidal one. Magnetic field lines are pinched locally and folded. As a result, a spherical magnetic bubble is formed in this process, in which the toroidal magnetic field is predominant.

The toroidal component of the magnetic fields is continuously generated by the twisting motion driven by the disk rotation. The disk angular momentum is transferred by this process. As a result, we do not see any rings that are supported by the centrifugal force.

For the model with an extremely weak field, we calculated model EH ($\alpha = 0.01$ and $\Omega_0 = 1$). In panel *f*, we plot the snapshot at $t = 0.7830\tau_{\rm ff}$ ($\tau = 4.53 \times 10^{-3}\tau_{\rm ff}$). The density distribution and magnetic field configuration show that the flow in the magnetic bubble becomes more complicated or turbulent in this model. Figure 7*f* shows that the magnetic field lines and flow velocities of model EH have spatially smaller scale variations than model DH in panel *e*. The shape of the bubble is more elongated than that formed in model DH. Distribution of toroidal field lines seems not to show any systematic pattern inside the bubble. The size of the bubble both in the z- and r-directions is smaller than those of models BH and DH. Thus, it is concluded that the size of the outflow region increases with increasing magnetic field strength α. Comparing these three models, it is shown that there are at least two types of outflows, that is, a laminar U-type flow in which fast-moving gas flows through a region whose shape resembles a capital letter U and a turbulent outflow in which the magnetic fields and the velocity change their directions in a small scale. For weak poloidal magnetic fields, the global flow pattern of the turbulent outflow looks like a capital letter I. Therefore, it is concluded that there are two patterns of outflows: the U-type flow for $\alpha \simeq 1$ and the I-type flow for $\alpha \ll 1$.

Plots similar to Figure 3*c* are shown in Figures 7*g* and 7*h* for models DH and EH, respectively. The centrifugal force–dominated region (region C), which is indicated by the asterisks, is found mainly near the disk, while departing from the disk, the magnetic force–dominated region (region M) indicated by the plus signs becomes predominantly distributed. This shows us that to launch the gas from the disk both the centrifugal force and the toroidal magnetic field gradient work, while the toroidal magnetic field gradient has an important role in expanding the bubble. That is, the magnetic energy stored inside the I-type flow drives the outflow motion. It should be noticed that this is completely different from Figure 3*c* with strong magnetic fields, in which regions M and C form a line, and along the line gas seems to be accelerated.

Calculating the plasma $\beta \equiv c_s^2\rho/[(B_z^2 + B_r^2 + B_\phi^2)/8\pi]$, the magnetic bubble or the I-type outflow shows $\beta < 1$, while the outer pseudodisk shows $10 < \beta < 100$ for model EH. This value is larger than that of model BH, which shows $\beta < 0.1$ in the outflow and $1 \lesssim \beta \lesssim 10$ in the disk. This difference comes from the fact that the initial magnetic field is weak ($\alpha = 0.01$) for model EH. However, it should be noticed that even though the initial magnetic field is weak, the magnetic field is amplified greatly from the seed field in the outflow region. A quarter of the outflow in volume is occupied by a gas of $\beta < 0.1$, which indicates that the magnetic field is important to the dynamics of the outflow. On the other hand, considering the poloidal magnetic field, the magnetic field lines are folded almost vertically in the magnetic bubble. In other words, a large part of the bubble is occupied by poloidal magnetic field lines dominated by B_z over B_r. This configuration is disadvantageous to the magnetocentrifugal acceleration mechanism (§ 3.2). In this case, the magnetic force (the magnetic pressure gradient) seems to accelerate the gas.

The core masses accumulated in $\tau \sim 4.5 \times 10^{-3}\tau_{\rm ff}$ are equal to $1.3c_s^3/(4\pi G)^{3/2}\rho_s^{1/2}$ for model BH, $0.87c_s^3/(4\pi G)^{3/2}\rho_s^{1/2}$ for model DH, and $0.65c_s^3/(4\pi G)^{3/2}\rho_s^{1/2}$ for model EH. This shows that the mass accretion rate, $\dot{M}_{\rm acc}$, is an increasing function of the initial magnetic field strength, α. This seems strange if we remember $\dot{M}_{\rm acc}$ is a decreasing function of the initial rotation speed, Ω_0, since both α and Ω_0 have the same effect of counterbalancing against self-gravity. This means that the mass inflow rate in the isothermal runaway collapse region, $(\dot{M}_{\rm in})_{\rm outermost}$, increases with increasing α. This seems to come from a number of reasons; that is, the initial cylindrical cloud becomes more massive with increasing α. Another reason is related to the characteristic wave speed in the magnetized medium. That is, the characteristic speed of the fast-mode MHD wave is equal to $(c_s^2 + B_0^2/4\pi\rho)^{1/2} = c_s(1 + \alpha)^{1/2}$ in the case where the wave is propagating perpendicular to the magnetic field lines. This implies that the mass inflow rates are proportional to the cube of the characteristic wave speed as $c_s^3(1 + \alpha)^{3/2}$, which leads to the accretion rates for these models as BH : DH : EH = 2.83 : 1.15 : 1.02. This is not inconsistent with the actual values.

4. DISCUSSION

4.1. *Evolution to Form the Second Core*

In the previous section, we introduced a simple polytrope above the critical density $\rho > \rho_{\rm A}$ except for model A. However, this is an approximation to see a long evolution. In this section, the evolution assuming the multiple polytrope (eq. [14]) is shown. Here, a further evolution later than that shown in Figures 1 and 2 is shown. In model R, we use the multiple polytrope to include combined effects such as dynamical compressional heating, radiative cooling through dust thermal emissions, and energy loss associated with the H_2 dissociation. This corresponds to the continuation of model A, but we consider here a more compact cloud as $\rho_s = 10^4$ H_2 cm^{-3}. It should be addressed that since ρ_s is assumed 100 times larger than other models, the size scale $H \simeq 1.05 \times 10^{17}(c_s/190\ \mathrm{m\ s^{-1}})(\rho_s/10^4\ \mathrm{H_2\ cm^{-3}})^{-1/2}$ cm is 10 times smaller than other models with $\rho_s = 10^2$ H_2 cm^{-3}.

The evolution up to the first core formation is similar to model A. After the equation of state becomes hard, $\rho > \rho_\mathrm{A}$, the collapse of the core slows down, and isothermal gas begins to accrete onto the core. In Figure 8*a*, we plot the structure represented in L6 just before the first core formation, $t = 0.7201\tau_\mathrm{ff}$.

Since the accretion continues, the mass of the first core increases with time, which leads to a quasi-static core collapse. The structure at this stage (at

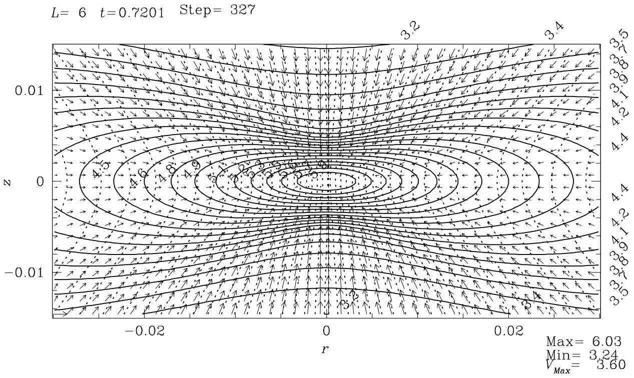

FIG. 8*a*

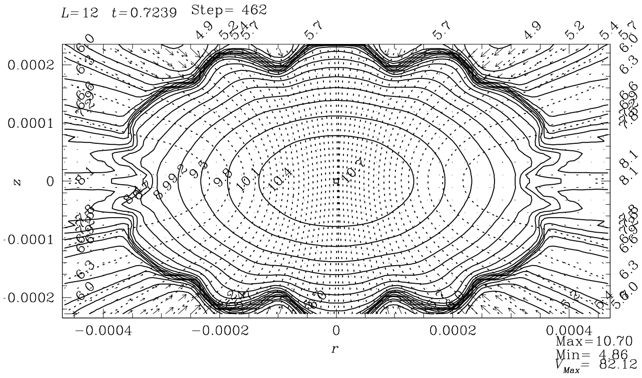

FIG. 8*b*

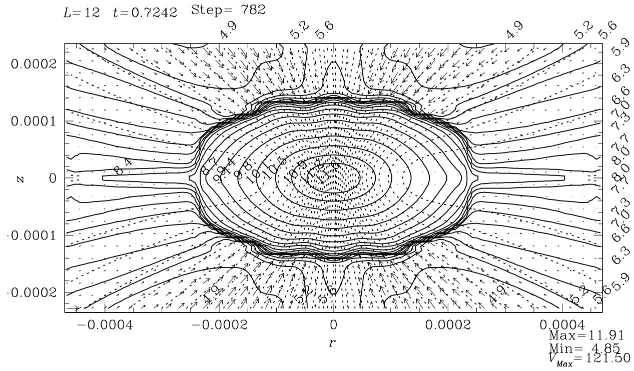

FIG. 8*c*

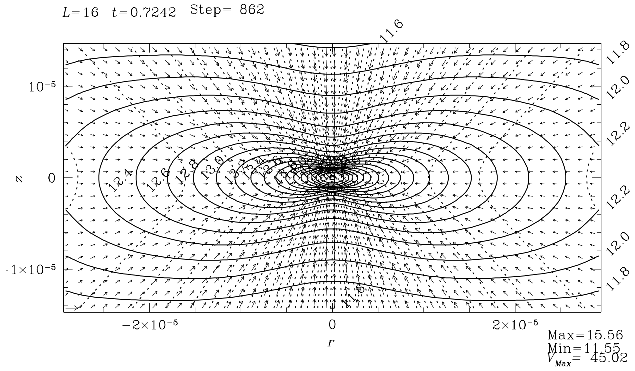

FIG. 8*d*

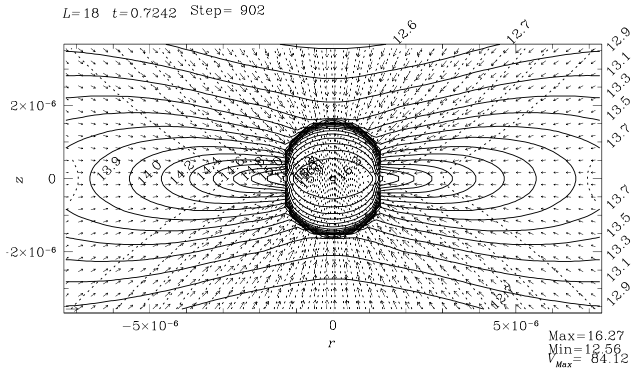

FIG. 8*e*

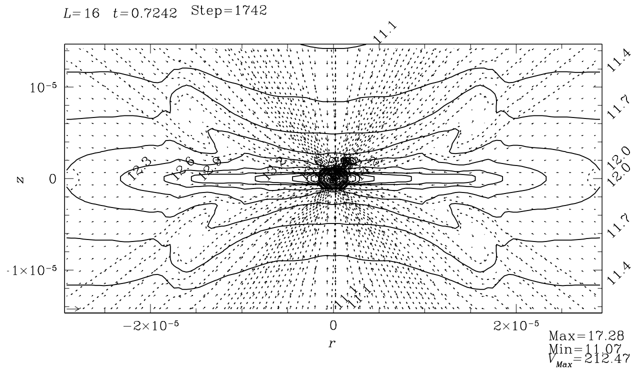

FIG. 8*f*

FIG. 8.—Evolution of model R. In this model, since ρ_s is assumed equal to 10^4 H_2 cm^{-3}, the size scale H is 10 times smaller than other models with $\rho_s = 10^2$ H_2 cm^{-3}. In (*a*), we plot the structure represented in L6 just before the first core formation $t = 0.7201\tau_\mathrm{ff}$. At $t = 0.7239\tau_\mathrm{ff}$ ($\tau = 3.8 \times 10^{-3}\tau_\mathrm{ff}$), the first core gradually contracts by the effect of continuous mass accretion (*b*). Finally, at $t = 0.724230\tau_\mathrm{ff}$ ($\tau = 4.132 \times 10^{-3}\tau_\mathrm{ff}$), the central density reaches ρ_B (*c*). After that, the second collapse begins. In this phase, flow is very similar to that realized in the isothermal runaway collapse phase. In (*d*), we plot the structure captured in L16 at $t = 0.724236\tau_\mathrm{ff}$ ($\tau = 4.138 \times 10^{-3}\tau_\mathrm{ff}$). After the central density exceeds ρ_C, another adiabatic core (the second core) is formed (*e*). By a similar mechanism for forming a bipolar outflow, a second outflow is formed around the second core (*f*). This is a snapshot of L16 at $t = 0.724237\tau_\mathrm{ff}$ ($\tau = 4.140 \times 10^{-3}\tau_\mathrm{ff}$). [*See the electronic edition of the Journal for a color version of this figure.*]

$t = 0.7239\tau_{\rm ff}$ or $\tau = 3.8 \times 10^{-3}\tau_{\rm ff}$) is shown in panel *b*. The radius of the first core shown in this panel is equal to $r \sim 3.5 \times 10^{-4}H \simeq 2.45(c_s/190\ {\rm m\ s^{-1}})(\rho_s/10^4\ {\rm H_2\ cm^{-3}})^{-1/2}$ AU. The curved boundary of the core is real.[4] This quasi-static contraction phase ends when the central density reaches $\rho_{\rm B}$.

The structure at this stage ($t = 0.724230\tau_{\rm ff}$ [$\tau = 4.132 \times 10^{-3}\tau_{\rm ff}$]) is plotted in panel *c*. Comparing this with panel *b*, both of which illustrate L12, it is clear that the adiabatic core is shrinking. After that, a second collapse begins. Since the thermal energy is lost by the process of the dissociation of H_2, the equation of state is assumed to be soft ($\gamma \simeq 1.1$) again. In this phase, the flow is very similar to that realized in the isothermal runaway collapse phase ($\rho_c < \rho_{\rm A}$). The similarity comes from the fact that the equations of state for both phases are soft ($\Gamma \simeq 1$). In panel *d*, we plot the structure represented in L16 at $t = 0.724236\tau_{\rm ff}$ ($\tau = 4.138 \times 10^{-3}\tau_{\rm ff}$), which represents the typical structure in the second-collapse phase. It should be realized that the flow pattern of the second collapse is very similar to the first collapse (the isothermal runaway collapse). This continues until the central density exceeds $\rho_c > \rho_{\rm C}$, beyond which another adiabatic core (the second core) is formed, shown in panel *e*. The size of the second core is equal to $\simeq 1.3 \times 10^{-6}H \sim 2\ R_\odot(c_s/190\ {\rm m\ s^{-1}})(\rho_s/10^4\ {\rm H_2\ cm^{-3}})^{-1/2}$. This meets a similar situation when the first adiabatic core is formed; that is, a central part of the gas obeys a harder equation of state and forms a quasi-static core, while the outer part obeys a softer equation of state and continues to collapse. The analogy between the first and the second core leads to an expectation of a bipolar outflow around the second core. In Figure 8*f*, it is shown the second outflow is formed around the second core. This is a snapshot of L16 at $t = 0.724237\tau_{\rm ff}$ ($\tau = 4.140 \times 10^{-3}\tau_{\rm ff}$), which resembles the structure seen in Figure 3*b*.

This model strongly indicates to us that there is another kind of outflow accelerated around the second core (the second outflow) besides that formed around the first core (the first outflow). The flow speed of the second outflow, $\sim 50c_s$, is much faster than that of the first outflow. This seems to come from the fact that the outflow occurs in circumstances forming a faster outflow; for example, the thermal speed near the second core is much faster, and the local gravitational potential is much deeper compared with the site where the first outflow is formed. Since the time span of the simulation shown here is restricted, we cannot trace the evolution further. However, the simulation predicts that at least two different outflows are formed, each of which is related to different types of adiabatic cores. Since the flow speed of the second outflow is much faster than that of the first outflow, the respective outflows correspond to the molecular bipolar outflow (the first outflow) and the fast neutral wind or the optical jets (the second outflow). The radial size of the outflow is approximately equal to $2 \times 10^{-5}H \sim 2.1 \times 10^{12}(c_s/190\ {\rm m\ s^{-1}})(\rho_s\ /10^4\ {\rm H_2\ cm^{-3}})^{-1/2}$ cm (=0.14 AU or 30 $R_\odot$). This indicates that optical jets are found inside molecular bipolar outflows.

In model R, we assume the ideal magnetohydrodynamics. However, the ionization fraction of high-density gas is quite low, and the electric conductivity decreases as collapse proceeds. Calculation of ionization equilibrium (Nakano & Umebayashi 1986) shows us that after $n_{\rm H} \gtrsim 10^{12}\ {\rm cm^{-3}}$, charged grains are more abundant than ions and become carriers of the electric currents. Since the mass-to-charge ratio of grains is much larger than that of ions, the electric conductivity decreases greatly, and the magnetic field decays mainly through Joule dissipation. Therefore, in the late phase of the first core (quasi-static contraction), the magnetic field in the core decreases its strength until the field configuration becomes force free. After the dissociation of H_2 begins, the temperature of the central region is high enough to achieve the thermal ionization of metals. Thus, in the second-collapse phase, coupling of magnetic fields is recovered. From these, the ideal MHD is consistent in the first- and the second-collapse phases. However, the magnetic flux density at the beginning of the second-collapse phases seems to be much weaker than that obtained here. As shown in § 3.5.2, when the poloidal magnetic field is weak, the flow pattern is different from the case where the magnetic energy is comparable to the thermal one. Therefore, if the magnetic flux is partly lost from the central part of the first core, a turbulent outflow around the second core seems to be formed similar to Figure 7*f*.

4.2. *Mass Inflow/Outflow Rate*

In this subsection, mass inflow/outflow rates and linear momentum outflow rates are seen more closely. The outflow mass-loss rate through the boundary of each grid level is calculated as

$$\dot{M}_{\rm out}({\rm L}n) = \int_{\text{boundary of L}n} \rho \max[\boldsymbol{v} \cdot \boldsymbol{n}, 0] dS\ , \qquad (31)$$

where $\boldsymbol{n}$ represents the unit vector outwardly normal to the surface. The integrand means that only the outwardly running mass flux is summed up. Similarly, the mass inflow rate is calculated as

$$\dot{M}_{\rm in}({\rm L}n) = \int_{\text{boundary of L}n} \rho \max[-\boldsymbol{v} \cdot \boldsymbol{n}, 0] dS\ . \qquad (32)$$

These rates are calculated for the respective levels of the nested grid system.

The time variations of mass inflow and outflow rates are illustrated for the respective models in Figure 9. The time (*horizontal axis*) is measured from the epoch of the core formation. Time variations, especially longer time variations, seen in the inflow rates are common for all panels. Just after core formation, the inflowing mass flux decreases with the distance from the center or from L11 to L6. This means that the inner part of the isothermal collapse region is well expressed by the Larson (1969)–Penston (1969) self-similar solution (Ogino, Tomisaka, & Nakamura 2000), which leads to a mass inflow rate of $47c_s^3/G$. Departing from the center, the approximation of the Larson-Penston solution becomes worse, and the inflow rate decreases. At $\tau \sim 4 \times 10^{-3}\tau_{\rm ff}$, the inflow rates for various surfaces converge to $\simeq 20c_s^3/G$, although intense outflow reduces the inflow rate below this value.

---

[4] To explore the reason why the surface of the core becomes wavy, we plot the angular rotation speed, which varies in the polytropic core. The ridge is formed mainly by fast-rotating gas, while the trough corresponds to slowly rotating gas. The angular momentum of the core is dependent on the efficiency of the angular momentum transport to the outflow. That is, core gas in a magnetic flux tube from which the strong outflow blows has a small angular momentum. Such a gas even shows counter rotation.

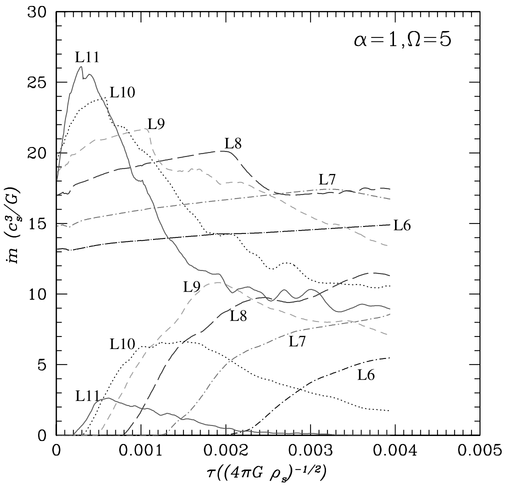

FIG. 9*a*

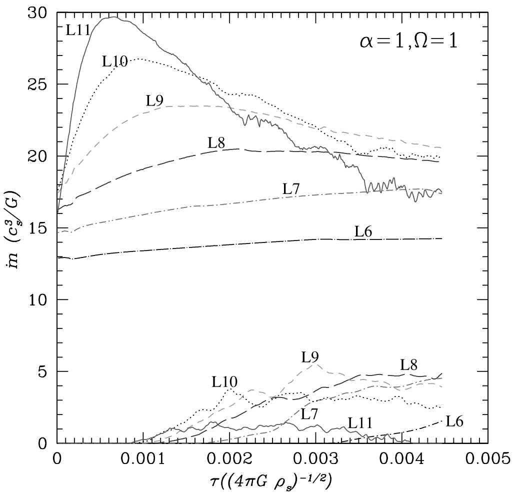

FIG. 9*b*

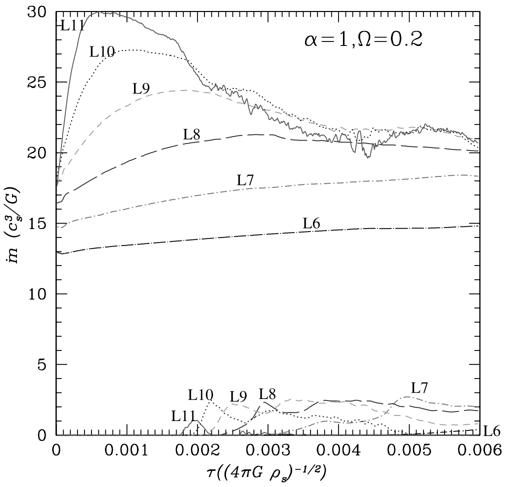

FIG. 9*c*

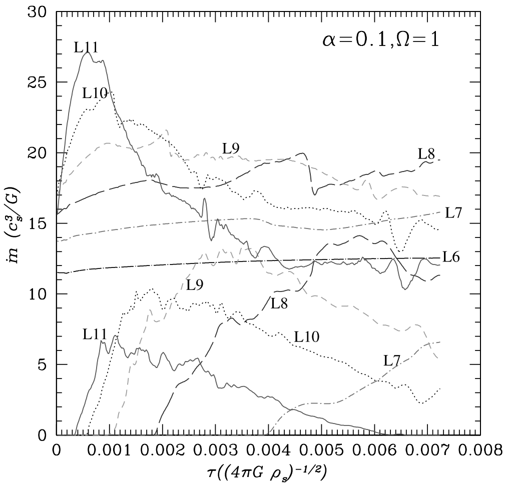

FIG. 9*d*

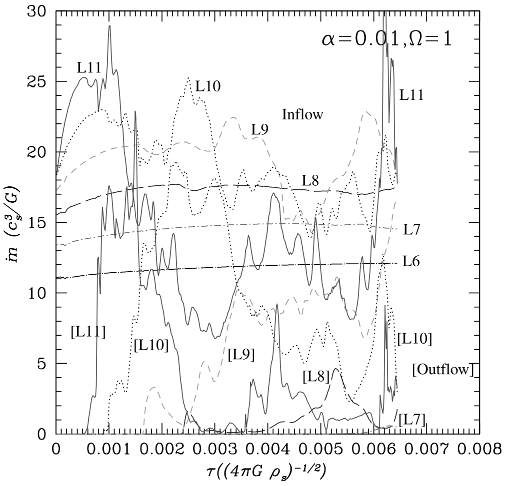

FIG. 9*e*

FIG. 9.—Mass inflow/outflow rates calculated at the boundaries of nested grid systems (eqs. [32] and [31]). Panels *a*–*e* correspond to models AH1, BH, CH, DH, and EH. The horizontal axis represents the time after the core formation. Levels at which the mass inflow/outflow rates are calculated are shown near the respective lines. We plot L11 as a solid line, L10 as a dotted line, L9 as a short-dashed line, L8 as a long-dashed line, L7 as a short-dash–dotted line, and L6 as a long-dash–dotted line. In panel *e*, to specify which line represents the outflow, we add brackets to the outflow rates. Inflow rates are larger than outflow rates for respective levels. [*See the electronic edition of the Journal for a color version of this figure.*]

We will see each model more closely. The mass outflow rate rises in the deeper levels (Ln with larger n) first, and this propagates to lower levels (Ln with smaller n). This indicates that the outflow region expands outwardly. Comparing models AH1 (panel *a*), BH (panel *b*), and CH (panel *c*), the effects of the initial rotation speed, Ω_0, are apparent. (1) With increasing Ω_0, the outflow begins earlier. (2) With increasing Ω_0, the mass outflow rate increases; although the ratio $\dot{M}_{\rm out}/\dot{M}_{\rm in}$ is equal to only $\sim$10% in model CH ($\Omega_0 = 0.2$), in model AH1 ($\Omega_0 = 5$), it attains $\sim$50%.

We compare models BH (panel *b*), DH (panel *d*), and EH (panel *e*) to see the effects of the initial magnetic field strength, α. This indicates that with decreasing α (from models BH to DH) the mass outflow rate increases. However, in model E, in which we assume extremely weak poloidal magnetic fields, the time variations in the mass inflow and outflow rates are rather chaotic and are led by the chaotic flow pattern realized in model EH (Fig. 7*f*). Averaging the rates as $\langle \dot{M} \rangle = \int_0^T \dot{M}\, dt/T$, the mass outflow rate of model EH is $\sim$20%–40% *smaller* than that of model DH. Considering the disk after rotating at a fixed angle, the disk of model EH can generate weaker toroidal magnetic fields than model DH, since model EH has only weak poloidal (source) magnetic fields. Therefore, it is reasonable that the mass outflow rate in model EH, $\langle \dot{M}_{\rm out} \rangle$, is smaller than that of model DH.

What about the increase in the mass outflow rate from models BH to DH? This is inconsistent with the above discussion. This increase seems related to the fact that the flow patterns of models BH and DH are different. That is, in model DH a magnetic bubble, in which magnetic field lines are folded and amplified, is formed, and the bubble expands. In contrast, in model BH, the gas is flowing outward along specific magnetic field lines, and outflowing gas moves through a region that looks like a capital letter U. The mass outflow rate seems larger in the magnetic bubble–type outflow than in the U-type outflow.

The linear momentum outflow rates are calculated by

$$\left|\frac{dMV}{dt}\right|_{\rm out}({\rm L}n) = \int_{\text{upper and lower boundaries of L}n} \rho v_z \times \max[\boldsymbol{v}\cdot\boldsymbol{n}, 0] dS\ , \qquad (33)$$

where we summed up the outflowing linear momentum in the z-direction through the upper and lower boundaries of Ln. Time variations of the momentum outflow rate are shown in Figure 10.

Figures 10*a*, 10*b*, and 10*c* have a prominent common feature in that the momentum outflow rates (dMV/dt) calculated at the boundaries of Ln for $n \leq 7$ are much larger than those of the boundaries of Ln for $n > 7$. This feature is common in models with $\alpha = 1$ (models AH1, AH2, BH, and CH). However, models with weaker magnetic fields do not show this feature. Recall the fact that models AH1, AH2, BH, and CH form the U-shaped outflow, and in contrast models DH and EH form the magnetic bubble or the I-type outflow. Difference in the momentum outflow rate seems to be related to the outflow pattern. In the laminar U-shaped outflow, the outflow is ejected with a rather wide opening angle and collimated to the symmetric axis. Since equation (33) counts the momentum passing the upper and lower boundaries, the outflow rate increases after the outflow is collimated, and the gas flows parallel to the z-axis. This occurs on the larger scale than L7.

Typical momentum outflow rates for molecular bipolar outflows observed with ^{12}CO $J = 2$–1 (Bontemps et al. 1996) are distributed between $\sim 10^{-4}\ M_\odot$ yr^{-1} km s^{-1} for objects associated with active Class 0 IR sources and $\sim 2 \times 10^{-6}\ M_\odot$ yr^{-1} km s^{-1} for objects associated with late Class I IR sources. This range corresponds to $320 c_s^4/G$–$6.5 c_s^4/G$, respectively, if we assume $c_s = 190$ m s^{-1}. Figure 10 shows us that the momentum outflow rate in the range from $\sim 10 c_s^4/G$ to $\sim 40 c_s^4/G$ is expected. Thus, the momentum outflow rates for almost all the CO bipolar outflow sources associated with low-mass young stellar objects are explained by our model except for the active early Class 0 sources.

Comparing models AH1, BH, and CH, it is shown that the momentum outflow rate increases with Ω_0. Comparing mass outflow and momentum outflow rates, models AH1, BH, and CH indicate that the momentum outflow rate is approximately proportional to the mass outflow rate, which means that the outflow speed is approximately equal irrespective of Ω_0. However, changing α is more complicated. Compare panels *b*, *d*, and *e*. As shown in Figure 9, model DH ($\alpha = 0.1$) shows a larger mass outflow rate than model BH ($\alpha = 1$). In contrast, as for the momentum outflow rate, the maximum rate of model BH is larger than that of model DH (Fig. 10). This means the outflow speed of model BH ($\alpha = 1$) is faster than that of model DH ($\alpha = 0.1$). Panel *e* shows that the momentum outflow rate has a chaotic time variation like the mass outflow rate (Fig. 9*e*) for model EH, which seems to correspond the turbulent outflow shown in Figure 7*f*.

Summarizing the effect of changing α:

1. The mass outflow rate increases with increasing α for $\alpha \lesssim 0.1$ but decreases after $\alpha \gtrsim 0.1$.
2. The outflow speed is an increasing function of α.
3. There are two distinctly different types of flow patterns: models with strong magnetic fields lead the U-shaped outflow, while the flow becomes turbulent for models with weak magnetic fields.

4.3. *Estimates of Angular Momentum*

Here, we intend to clarify where the outflow is ejected. In the runaway collapse phase, the rotational motion is relatively unimportant. After core formation, the rotational motion increases, especially around the first core. This occurs near the centrifugal radius, which is defined for a gas with specific angular momentum j as

$$R_{\rm c} = c_{\rm c}\frac{j^2}{GM}\ , \qquad (34)$$

where M denotes the mass inside the radius $R_{\rm c}$ and $c_{\rm c}$ represents a numerical factor of the order of unity. Considering a self-similar solution for the runaway collapse phase (Saigo & Hanawa 1998), the specific angular momentum j is proportional to M. This is confirmed by numerical calculations as the mass and the specific angular momentum are proportional to each other (see Fig. 2 of Tomisaka 2000). This is valid only at the core formation epoch, and the core loses its angular momentum after core formation. Further, a uniform-density cylinder that is rotating with a uniform rotation speed ω has a j-distribution proportional to M.

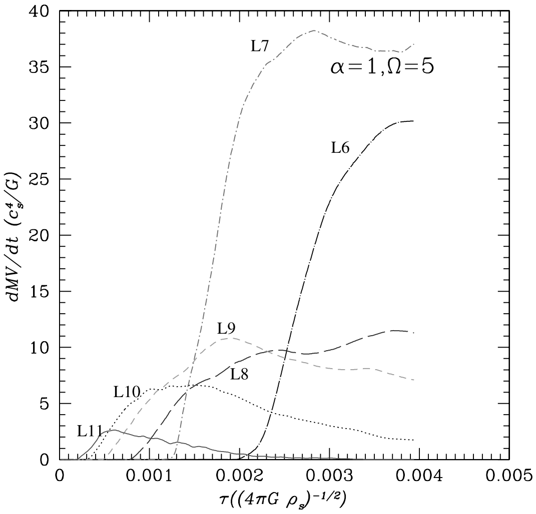

FIG. 10*a*

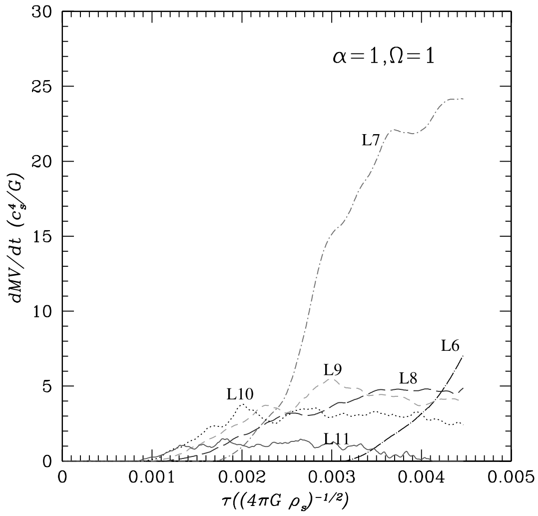

FIG. 10*b*

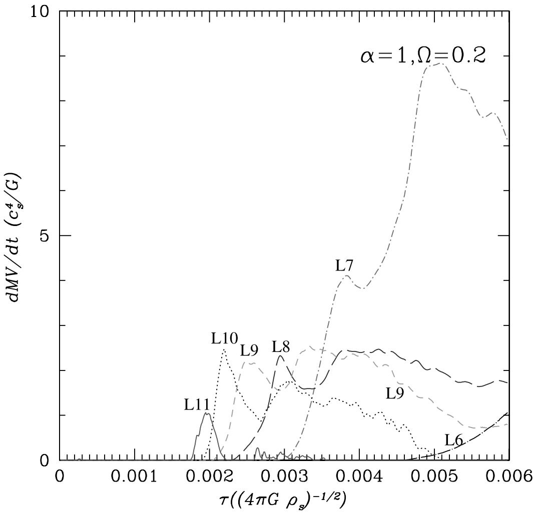

FIG. 10*c*

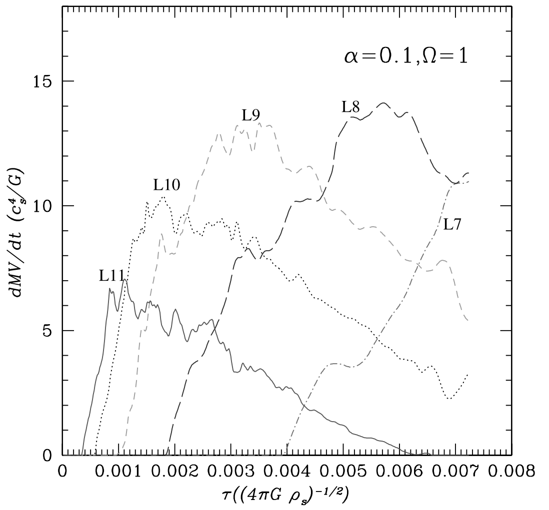

FIG. 10*d*

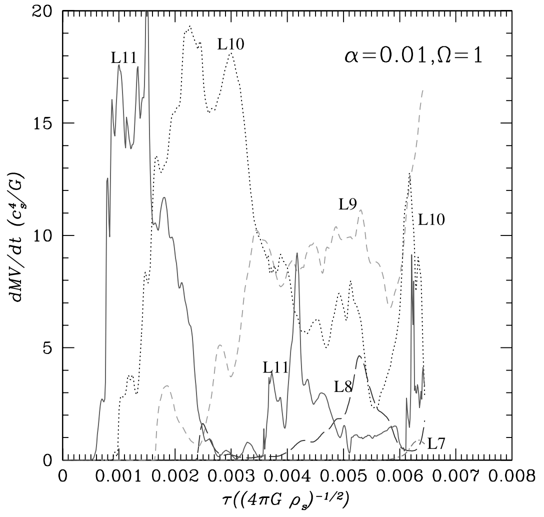

FIG. 10*e*

FIG. 10.—Linear momentum outflow rates calculated at the upper and lower boundaries of nested grid systems (eq. [33]). Panels *a*–*e* correspond to models AH1, BH, CH, DH, and EH. The horizontal axis represents the time after core formation. Levels at which the linear momentum outflow rates are measured are shown near the respective lines. We plot L11 as a solid line, L10 as a dotted line, L9 as a short-dashed line, L8 as a long-dashed line, L7 as a short-dash–dotted line, and L6 as a long-dash–dotted line. [*See the electronic edition of the Journal for a color version of this figure.*]

Assuming $j = qGM/c_s$ (q is a numerical factor), the centrifugal radius is written

$$R_c = c_c \frac{q^2 GM}{c_s} . \tag{35}$$

As shown in § 3, the angular momentum is redistributed in one magnetic flux tube, after the core is formed and the outflow begins to flow. That is, gas near the disk surface obtains a large amount of the specific angular momentum, but that near the disk midplane loses the angular momentum. If the gas near the disk surface has an angular momentum of $j_+ > j$ in consequence of the angular momentum redistribution, the condition that the effective potential at the centrifugal radius

$$\Phi(R_c) = -\frac{GM}{R_c} + \frac{j_+^2}{2R_c^2} \tag{36}$$

is larger than or equal to zero leads to a minimum angular momentum of

$$j_+ \geq (2c_c)^{1/2} j , \tag{37}$$

above which the gas with the specific angular momentum can escape from the gravitational well. Since the angular momentum transfer occurs mainly after core formation, the specific angular momentum j expected for a magnetized cloud is comparable to that of the nonmagnetized one (j) *at the core formation epoch*. After the core formation epoch, because of the angular momentum redistribution, j of the gas near the disk surface increases. Equation (37) shows us that if the specific angular momentum of such a gas exceeds $(2c_c)^{1/2} j$, the excess centrifugal force can drive the gas outward. The fact that the factor $(2c_c)^{1/2} \simeq 1$ is not too large seems to ensure the ejection of the outflow by this mechanism.

5. SUMMARY

We have explored the evolution of a magnetized interstellar cloud rotating around the symmetric axis. Following the change in the equation of state of the interstellar gas (Tohline 1982), the cloud experiences several phases before going to a star, that is, the isothermal runaway collapse, the slowly contracting core composed of the molecular hydrogen (the first core), the second runaway collapse in the high-density gas where the dissociation of hydrogen molecules proceeds, and finally, the second core that is made up of the atomic hydrogen. The magnetized cloud forms pseudodisks in which the first and the second runaway collapses occur. The pseudodisks are threaded by the magnetic field lines running perpendicularly to the disk. In the pseudodisk, a number of fast- and slow-mode MHD shock pairs are formed whose wave fronts are extending parallel to the disk. Just after the first core is formed at the center, an accretion shock front appears that surrounds the core, through which the supersonic inflow motion is decelerated. While the first and second cores are slowly contacting, the outer pseudodisks continue to contract. Just outside the accretion shock front, the infall motion is accelerated, and thus rotational motion becomes important from the conservation of angular momentum. By the effect of rotational motion, the toroidal magnetic fields and the poloidal electric currents are amplified, which bring a strong magnetic torque. The magnetic torque leads the angular momentum transfer from the midplane to the surface of the pseudodisk. This is actually confirmed by the fact that in the outflow region the centrifugal force and the magnetic pressure gradient of the toroidal magnetic fields are dominant over the thermal pressure gradient. This is the origin of the outflow found in star-forming regions. Large-scale bipolar molecular outflows are made outside of the first core, while optical jets and fast neutral winds are expected to be accelerated outside of the second core. Matter losing its excess angular momentum continues to contract further to form a star.

The author would like to thank an anonymous referee who provided useful comments to improve the paper. This work was supported partially by the grants-in-aid (11640231 and 10147105) from MEXT (the Ministry of Education, Culture, Sports, Science and Technology). Numerical calculations were carried out by the Fujitsu VPP5000 at the Astronomical Data Analysis Center, the National Astronomical Observatory, an interuniversity research institute of astronomy operated by MEXT, Japan.

REFERENCES

Basu, S., & Mouschovias, T. C. 1994, ApJ, 432, 720
———. 1995, ApJ, 452, 386
Bate, M. R. 1998, ApJ, 508, L95
Bentz, W. 1984, A&A, 139, 378
Berger, M. J., & Colella, P. 1989, J. Comput. Phys., 82, 64
Berger, M. J., & Oliger, J. 1984, J. Comput. Phys., 53, 484
Blandford, R. D., & Peyne, D. G. 1982, MNRAS, 199, 883
Bodenheimer, P., Tohline, J. E., & Black, D. C. 1980, ApJ, 242, 209
Bontemps, S., Andre, P., Terebey, S., & Cabrit, S. 1996, A&A, 311, 858
Boss, A. P. 2000, ApJ, 545, L61
———. 2001, ApJ, 551, L167
Ciolek, G. E., & Basu, S. 2000, ApJ, 529, 925
Dorfi, E. 1982, A&A, 114, 151
———. 1989, A&A, 225, 507
Evans, C. R., & Hawley, J. F. 1988, ApJ, 332, 659
Fiedler, R. A., & Mouschovias, T. C. 1992, ApJ, 391, 199
———. 1993, ApJ, 415, 680
Goodman, A. A., Jones, T. J., Lada, E. A., & Myers, P. C. 1992, ApJ, 399, 108
———. 1995, ApJ, 448, 748
Gustafsson, I. 1978, BIT, 18, 142
Hayashi, C. 1987, in IAU Symp. 115, Star Forming Regions, ed. M. Peimbert & J. Jugaku (Dordrecht: Reidel), 403
Heyer, M. H., et al. 1987, ApJ, 321, 855
Klein, R. I., Fisher, R. T., McKee, C. F., & Truelove, J. K. 1999, in Numerical Astrophysics, ed. S. M. Miyama, K. Tomisaka, & T. Hanawa. (Boston: Kluwer), 131
Kudoh, T., Matsumoto, R., & Shibata, K. 1998, ApJ, 508, 186
Larson, R. B. 1969, MNRAS, 145, 271
Loren, R. B. 1989, ApJ, 338, 902
Masunaga, H., & Inutsuka, S. 1999, ApJ, 510, 822
Matsumoto, T., Hanawa, T., & Nakamura, F. 1997, ApJ, 478, 569
Matsumoto, T., Nakamura, F., & Hanawa, T. 1994, PASJ, 46, 243
Meijerink, J. A., & van der Vorst, H. A. 1977, Math. Comput., 31, 148
Mouschovias, T. C., & Morton, S. A. 1991, ApJ, 371, 296
———. 1992, ApJ, 390, 144
Nakamura, F., Hanawa, T., & Nakano, T. 1995, ApJ, 444, 770
Nakamura, F., Matsumoto, T., Hanawa, T., & Tomisaka, K. 1999, ApJ, 510, 274
Nakano, T., & Umebayshi, T. 1986, MNRAS, 218, 663
Narita, S., Hayashi, C., & Miyama, S. M. 1984, Prog. Theor. Phys., 72, 1118
Norman, M. L., Wilson, J. R., & Barton, R. T. 1980, ApJ, 239, 968
Norman, M. L., & Winkler, K.-H. A. 1986, in Astrophysical Radiation Hydrodynamics, ed. K.-H. A. Winkler & M. L. Norman (NATO ASI Ser. C, 188; Dordrecht: Reidel), 187
Ogino, S., Tomisaka, K., & Nakamura, F. 1999, PASJ, 51, 637
Ohashi, N., Lee, S. W., Wilner, D. J., & Hayashi, M. 1999, ApJ, 518, L41

Penston, M. V. 1969, MNRAS, 144, 425
Phillips, G. L. 1986a, MNRAS, 221, 571
———. 1986b, MNRAS, 222, 111
Saigo, K., & Hanawa, T. 1998, ApJ, 493, 342
Scott, E. H., & Black, D. C. 1980, ApJ, 239, 166
Shu, F. H. 1977, ApJ, 214, 488
Stodółkiewicz, J. S. 1963, Acta Astron., 13, 30
Stone, J. M., & Norman, M. L. 1992, ApJS, 80, 753
Tohline, J. E. 1982, Fundam. Cosmic Phys., 8, 1
Tomisaka, K. 1995, ApJ, 438, 226
———. 1996, PASJ, 48, 701
———. 1998, ApJ, 502, L163
———. 2000, ApJ, 528, L41
Tomisaka, K., & Bregman, J. N. 1993, PASJ, 45, 513
Tomisaka, K., Ikeuchi, S., & Nakamura, T. 1990, ApJ, 362, 202
Truelove, J. K., Klein, R. I., McKee, C. F., Holliman, J. H., II, Howell, L. H., & Greenough, J. A. 1997, ApJ, 489, L179
Truelove, J. K., Klein, R. I., McKee, C. F., Holliman, J. H., II, Howell, L. H., Greenough, J. A., & Woods, D. T. 1998, ApJ, 495, 821
Tsuribe, T., & Inutsuka, S. 1999a, ApJ, 523, L155
———. 1999b, ApJ, 526, 307
Ustyugova, G. V., Koldoba, A. V., Romanova, M. M., Chechetkin, V. M., & Lovelace, R. V. E. 1999, ApJ, 516, 221
van Leer, B. 1977, J. Comput. Phys., 23, 276
Whitworth, A., & Summers, D. 1985, MNRAS, 214, 1
Wood, D. 1982, MNRAS, 199, 331